LANGMUIR

pubs.acs.org/Langmuir Article

Probing IgG1 F_C-Multimodal Nanoparticle Interactions: A Combined Nuclear Magnetic Resonance and Molecular Dynamics Simulations Approach

Ronak B. Gudhka, Mayank Vats, Camille L. Bilodeau, Scott A. McCallum, Mark A. McCoy, David J. Roush, Mark A. Snyder, and Steven M. Cramer*



Cite This: Langmuir 2021, 37, 12188-12203



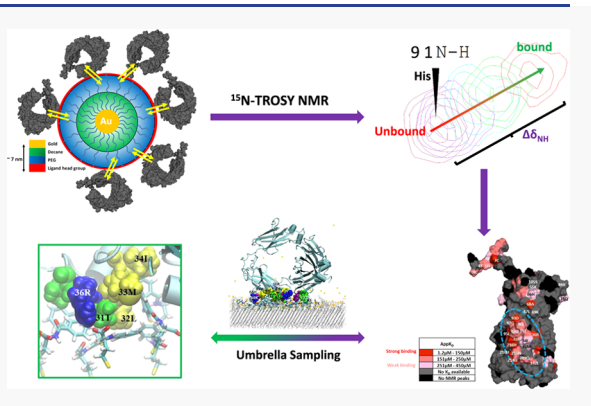
ACCESS

Metrics & More

Article Recommendations

Supporting Information

ABSTRACT: In this study, NMR and molecular dynamics simulations were employed to study IgG1 F_C binding to multimodal surfaces. Gold nanoparticles functionalized with two multimodal cation-exchange ligands (Capto and Nuvia) were synthesized and employed to carry out solution-phase NMR experiments with the F_C . Experiments with perdeuterated ¹⁵N-labeled F_C and the multimodal surfaces revealed micromolar residue-level binding affinities as compared to millimolar binding affinities with these ligands in free solution, likely due to cooperativity and avidity effects. The binding of F_C with the Capto ligand nanoparticles was concentrated near an aliphatic cluster in the C_H2/C_H3 interface, which corresponded to a focused hydrophobic region. In contrast, binding with the Nuvia ligand nanoparticles was more diffuse and corresponded to a large contiguous positive electrostatic potential region on the side face of the F_C . Results



with lower-ligand-density nanoparticles indicated a decrease in binding affinity for both systems. For the Capto ligand system, several aliphatic residues on the F_C that were important for binding to the higher-density surface did not interact with the lower-density nanoparticles. In contrast, no significant difference was observed in the interacting residues on the F_C to the high- and low-ligand density Nuvia surfaces. The binding affinities of F_C to both multimodal-functionalized nanoparticles decreased in the presence of salt due to the screening of multiple weak interactions of polar and positively charged residues. For the Capto ligand nanoparticle system, this resulted in an even more focused hydrophobic binding region in the interface of the $C_H 2$ and $C_H 3$ domains. Interestingly, for the Nuvia ligand nanoparticles, the presence of salt resulted in a large transition from a diffuse binding region to the same focused binding region determined for Capto nanoparticles at 150 mM salt. Molecular dynamics simulations corroborated the NMR results and provided important insights into the molecular basis of F_C binding to these different multimodal systems containing clustered (observed at high-ligand densities) and nonclustered ligand surfaces. This combined biophysical and simulation approach provided significant insights into the interactions of F_C with multimodal surfaces and sets the stage for future analyses with even more complex biotherapeutics.

1. INTRODUCTION

Multimodal (MM) ion-exchange (IEX) chromatography has been shown to have enhanced selectivity as compared to traditional ion exchangers due to the multiple interactions (electrostatic, hydrophobic, aromatic, and/or hydrogen bonding) that these ligands can have with a given solute. ¹⁻⁷ The impact of chemistry, solvent exposure, and presentation of functional groups and linkers have been examined and shown to affect selectivities in these chromatographic systems. ⁸⁻¹⁰ Further, the utility of MM chromatography has been demonstrated for important industrial monoclonal antibody (mAb) applications. ^{11,12}

Ligand-induced chemical shift perturbations (CSPs) in nuclear magnetic resonance (NMR) have been employed to identify ligand binding regions on proteins 13 and to determine the residue-level binding affinity. 14-16 We have employed two-

dimensional heteronuclear single quantum coherence (2D-HSQC) NMR experiments to identify binding sites of both IEX and MM IEX ligands on the protein ubiquitin and its mutants^{17,18} and to evaluate the effects of urea on these preferred binding regions.¹⁹

NMR has also been employed alone or in combination with other techniques to examine protein binding to surfaces. Engel et al.²⁰ employed hydrogen—deuterium exchange (HDX) in

Received: August 8, 2021
Revised: September 28, 2021
Published: October 11, 2021





concert with 2D NMR to study the conformational changes associated with the binding of α -lactalbumin to polystyrene nanospheres. Gagner et al.²¹ used NMR in combination with circular dichroism (CD) to examine conformational changes of lysozyme and α -chymotrypsin upon binding to amino acid-functionalized gold nanoparticles (Au NPs). Shrivastava et al.²² employed NMR in concert with mass spectrometry (MS) to identify interacting residues and binding orientations of acylphosphatase to different-sized silica NPs.

Multiple studies have employed self-assembled monolayers (SAMs) in concert with NPs for studying protein—ligand interactions. $^{23-26}$ You et al. 24 employed Au NPs functionalized with SAMs presenting amino acids for examining conformational changes on the surface of chymotrypsin upon adsorption. De et al. 25 extended this study to evaluate the binding of α chymotrypsin, histone, and cytochrome c to these amino acid-functionalized Au NPs. We have identified preferred MM interaction sites on ubiquitin using NMR with MM-functionalized Au NPs. 26

While a large body of literature exists on describing protein binding in single-mode interaction chromatographic systems,²⁷⁻³¹ work in understanding the interactions of proteins in MM systems at the molecular level is less pronounced. Zhang et al.³² performed a series of molecular dynamics (MD) simulations to study the changes in the binding orientation of a β-barrel protein on hydrophobic charge induction chromatography (HCIC) surfaces as a function of salt concentration. Yu et al.³³ employed coarse-grained simulations to investigate the preferred binding orientation of lysozyme on a HCIC surface at different ligand densities under a range of salt concentrations. We have employed chromatographic experiments in concert with NMR and MD simulations with a ubiquitin mutant library to demonstrate the synergistic effects of multiple modalities in MM ligands, cooperativity between clusters of residues on the protein surface, and their impact on protein selectivity.¹⁷ We have also used NMR^{18,19} and coarse-grained modeling strategies^{34–36} to identify preferred binding hotspots on the protein surface and to shed light on the role of electrostatic and water-mediated interactions on the binding affinities of MM ligands to proteins. A combination of atomic force microscopy (AFM) and MD simulations has also been used to validate a hypothesized preferred orientation for ubiquitin and to quantify the interaction energy with MM surfaces.³⁷

Recent work in our group has evaluated the domain contributions of mAb binding in MM chromatography using linear gradient chromatography with different fragments and protein surface property analysis. This work has demonstrated a shift in domain dominance depending on the surface properties of the mAb, resin type, and the operating pH. 38,39 Gagnon et al. 40 have shown that the binding of the F_C domain was driven primarily by calcium chelation interactions in hydroxyapatite (HA) chromatography. Lin et al.41 employed molecular simulations to identify preferred binding sites of an HCIC ligand on a single-chain F_C fragment. This study was then extended to HCIC ligands on surfaces to evaluate liganddensity effects and to elucidate the binding mechanisms of F_C in these systems at various pH conditions. 42 We have recently shown that the MM ligands in free solution have preferential interaction sites in the hinge region and in the C_H2/C_H3 interface on the F_C surface and that the binding affinities were in the mM range. ⁴³ While this study showed preferred MM

interaction sites on the F_C surface, it did not account for protein binding to MM surfaces.

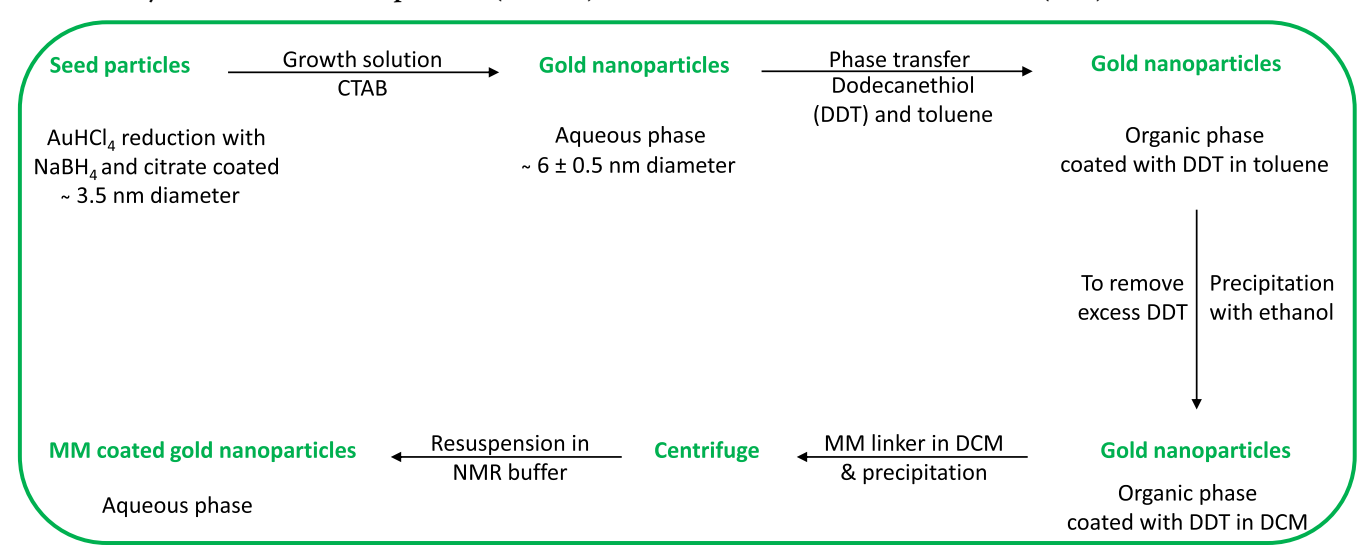
In the current work, we extend our previous work with small model proteins to the more complex F_C domain, which is conserved across a given class of antibodies using a combination of NMR and MD simulations to examine the interactions of the F_C with MM surfaces. First, we functionalize Au NPs with SAMs to develop a pseudo-solid-state resin system that mimics chromatographic surfaces and is amenable to NMR with the F_C. Transverse relaxation optimized spectroscopy (15N-TROSY) NMR titration experiments are then carried out using perdeuterated ¹⁵N-labeled F_C with both low- and high-density MM-functionalized NPs to identify primary binding sites on the protein and to obtain residuespecific binding affinities to these surfaces. These NMR experiments are also performed in the presence of salt to gain more insights into the nature of interactions in these systems. We also examine the NMR results as they compare to the protein surface property maps to develop a deeper understanding of the relation between the binding regions and patches on the protein surface. Finally, we employ MD simulations to provide further insights into the adsorption of the F_C molecule in these different MM systems. MM ligandimmobilized SAM surfaces have been shown to present patterned surfaces with patches of charge and hydrophobicity in the absence of a protein.⁴⁴ Here, we examine the impact of this ligand self-association phenomenon on protein adsorption by examining the intermolecular interactions and mechanisms occurring during binding of the F_C to these different MM ligand surfaces.

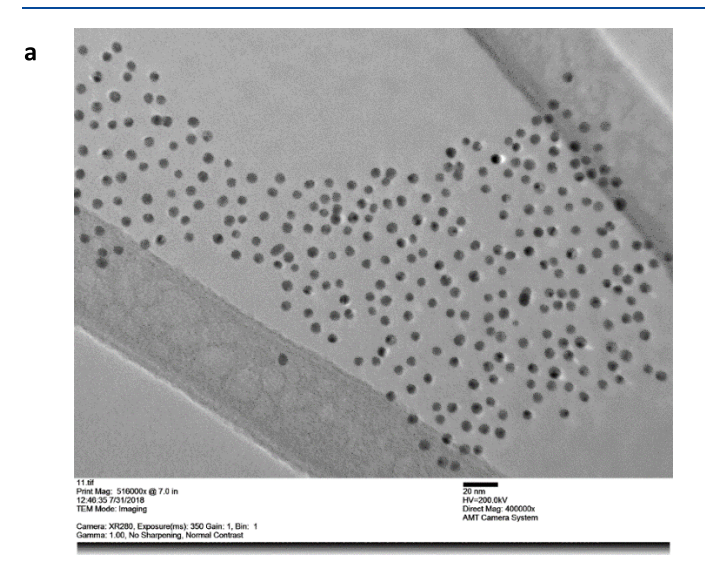
2. MATERIALS AND METHODS

2.1. Materials. Perdeuterated ¹⁵N-labeled IgG1 F_C domain (residues 1-228 corresponding to residues 220-447 in the IgG1) expressed in E. coli was provided by Merck & Co., Inc. (Kenilworth, NJ). Disposable Zeba spin desalting columns (7K MWCO, 0.5 mL) were purchased from Thermo Fisher Scientific (Waltham, MA). Sodium acetate, 4-amino hippuric acid, acetic acid, sodium azide, tetrahydrofuran (THF), sodium hydrogen phosphate, sodium dihydrogen phosphate, trifluoroacetic acid (TFA), gold chloride trihydrate salt, sodium borohydride, sodium citrate, potassium iodide, cetyl trimethyl ammonium bromide (CTAB), dodecanethiol (DDT), dichloromethane (DCM), toluene, reagent alcohol, acetonitrile (ACN), and hydrochloric acid were purchased from Sigma-Aldrich (St. Louis, MO). N-Benzoyl lysine was purchased from Chem-Impex international (Wood Dale, IL). Hexaethylene glycol thiols terminated with N-hydroxysuccinimide (NHS) ester groups were purchased from ProChimia Surfaces (Gdynia, Poland). Bruker microbore NMR sample tubes were purchased from Norell (Morganton, NC). Acquity high-performance liquid chromatography (HPLC) protein C18 column was purchased from Waters Corporation (Milford, MA).

2.2. Gold Nanoparticle Synthesis and Functionalization with MM Linkers. 2.2.1. Synthesis of MM Linker. The MM linker synthesis protocol was adapted from Srinivasan et al. 26 Briefly, 40 μ mol of NHS ester was dissolved in 100 μ L of THF. The MM ligand head groups, N-benzoyl lysine and 4-amino hippuric acid, were employed to synthesize the Capto and Nuvia linkers, respectively, and were dissolved in a 5 mL phosphate buffer saline (PBS) at a 20x molar excess of the ester. The ester solution was added to the MM ligand solution, and the resulting mixture was allowed to react for 36 h at room temperature. The final MM linker was purified from unreacted ligands using C_{18} reverse-phase liquid chromatography (RPLC). The mixture was loaded onto the column in buffer A (DI water with 0.1% v/v TFA) followed by a step gradient to 20% buffer B (95% v/v ACN in DI water with 0.1% v/v TFA) to elute the unreacted ligands. The MM linkers were eluted with a step change to 100% buffer B and

Scheme 1. Synthesis of Gold Nanoparticles (Au NPs) and Functionalization with Multimodal (MM) Linkers





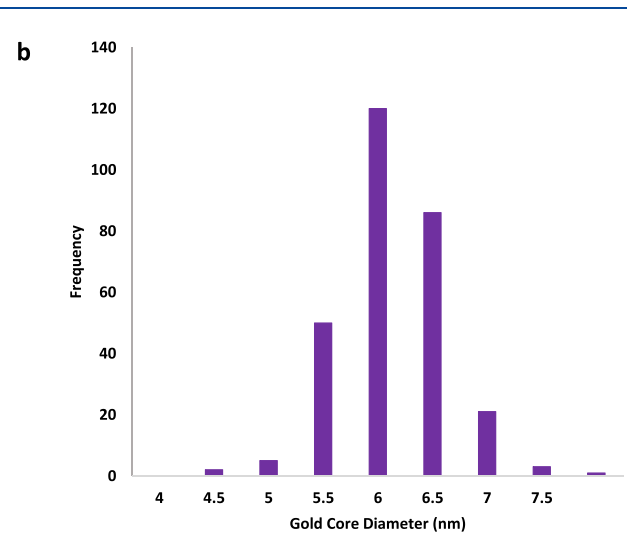


Figure 1. Representative (a) transmission electron microscopy (TEM) image of "Nuvia ligand" high-density NPs and (b) corresponding frequency distribution of the gold core.

collected with a purity > 80%. The ACN was evaporated using a rotavap, and the dried MM linker (liquid) was either immediately used to functionalize Au NPs or stored at $-20~^{\circ}$ C.

2.2.2. Synthesis of Gold Nanoparticles. The Au NP synthesis protocol was adapted from Jana et al. 45 Briefly, a two-phase approach was employed for the synthesis of MM-functionalized Au NPs, as shown in Scheme 1. The seed nanoparticles were prepared by adding 0.6 mL of freshly prepared 0.1 M sodium borohydride solution to a 20 mL mixture of 0.25 mM solution of gold chloride and sodium citrate under constant stirring. The solution was allowed to stir for 10 min for the synthesis of seed particles. The size and monodispersity of seed particles were confirmed by dynamic light scattering (DLS) (Wyatt DynaPro dynamic light scattering instrument, Wyatt Technology Corporation, CA). The seed particles were immediately employed for the next steps. One milliliter of 0.1 M ascorbic acid was added to the growth solution (15 mL of 2.5 mM gold chloride, 0.8 M CTAB) under constant stirring followed by the addition of $50\ mL$ of seed particles. After 10 min of constant stirring, ~14 nm diameter monodispersed Au NPs were obtained. The morphology and particle size of the NPs were measured using transmission electron microscopy (TEM) (JEOL JEM-2011 Transmission Electron Microscopy, JEOL USA, Inc., MA) and DLS, respectively.

For aqueous-to-organic phase transfer of Au NPs, first 650 μ L of DDT was added to the NPs under constant stirring at a 10× molar excess of gold salt followed by the addition of 1.3 mL of 0.1 M potassium iodide solution. After 1 min, ~5 mL of toluene was added to the solution under constant stirring. Immediately, the toluene layer visibly turned dark red color and the water phase became transparent, indicating transfer of the NPs from the aqueous to the organic phase. Au NPs were then separated from the aqueous phase and were precipitated using 250 mL of ethanol. The resulting solution was stored at $-80~\rm ^{\circ}C$ for at least 4 h for complete precipitation of the NPs prior to 0.22 μ m filtration. The filtered NPs were washed twice with ethanol and then resuspended in ~3 mL of DCM. The resulting NPs were then functionalized with MM linkers, as described below.

2.2.3. Functionalization of Gold Nanoparticles with MM Linkers. MM-functionalized Au NPs were synthesized by a place exchange reaction of DDT with MM linkers on the NP surface. The MM linkers that were previously dissolved in DCM were added to the NP solution at a 10x molar excess of the theoretical maximum (assuming $\sim\!\!4$ ligands/nm²) 57 linker concentration. The resulting solution was mixed on an end-to-end rotator for at least 72 h at room temperature. The MM-functionalized NPs were then precipitated from the solution by adding hexane at a 5x v/v excess of DCM. The resulting NP suspension was centrifuged at a low speed (<1500 rcf) for 2 min. The

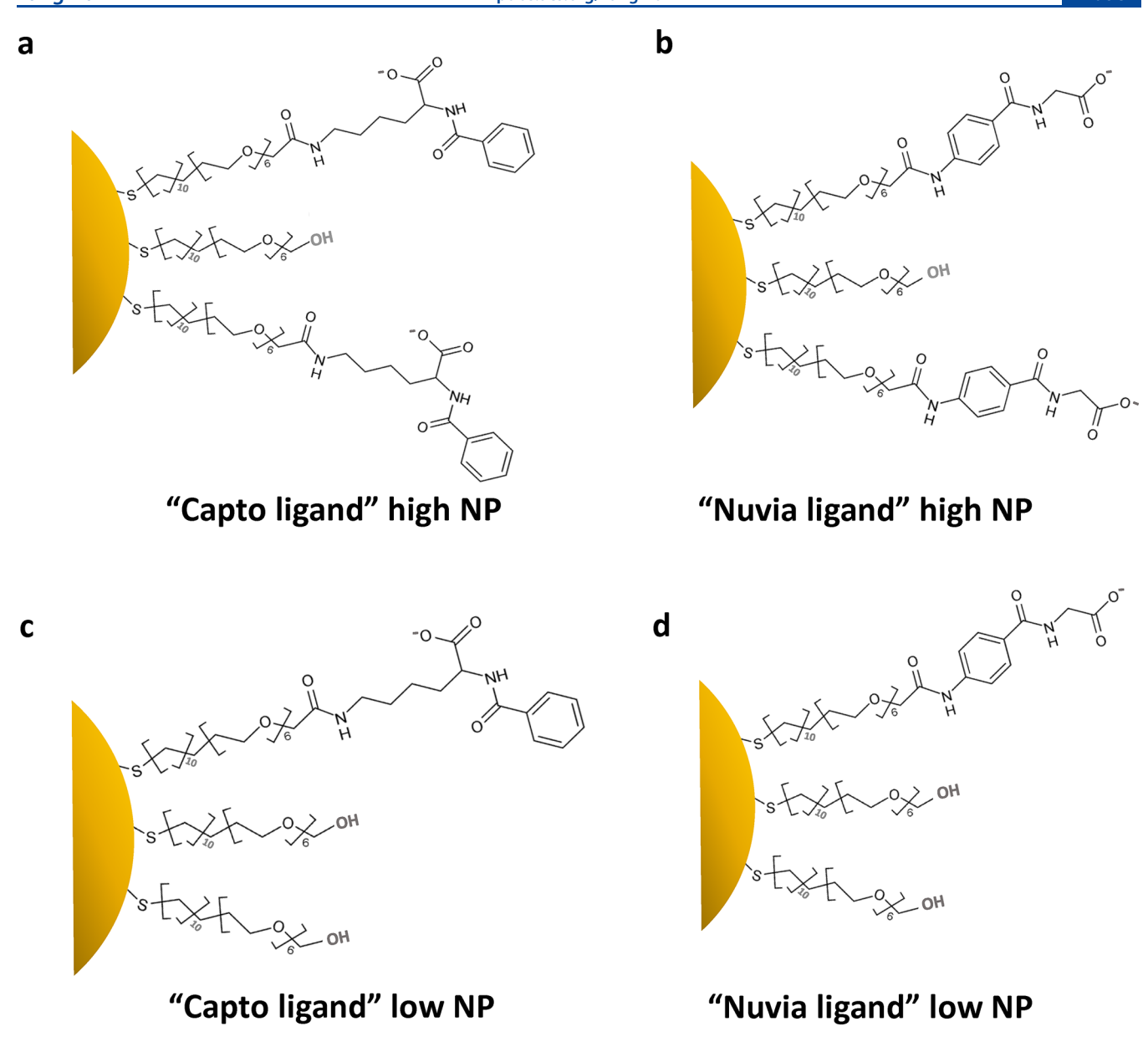


Figure 2. Self-assembled monolayers (SAMs) presenting MM ligands on gold nanoparticles (Au NPs) at different ligand densities. (a) "Capto ligand" high density, (b) "Nuvia ligand" high density, (c) "Capto ligand" low density, and (d) "Nuvia ligand" low density.

supernatant containing the excess of free ligand was then removed, and the NPs were washed twice with hexane and then dried under air in a fume hood for 3–5 min. The dried NPs were resuspended in the NMR buffer (10 mM sodium acetate, pH 5.0, 10% D_2O , and 0.02% sodium azide) and evaluated using NMR to detect the presence of a free linker in the solution. When necessary, the suspended NPs were buffer-exchanged with the NMR buffer using a 100 kDa centrifugal filter to remove any remaining free linkers from the solution.

The concentration of gold in the NP samples was measured using inductively coupled plasma mass spectrometry (ICPMS). The morphology and size of the functionalized NPs were confirmed by TEM (Figure 1a,b) and DLS (Figure S1a), respectively. The ligand density of MM linkers on Au NPs was controlled by varying the ratio of MM and hydroxyl linkers (HS-C₁₁-OEG₆-OH; Figure 2) in solution during the functionalization step, and the concentration of the MM linker in NP solution was determined using NMR. Au NPs were functionalized with MM linkers at high (~1 ligand/nm²) and low (~0.3 ligand/nm²) ligand densities, and the density was confirmed by the method described by Srinivasan et al. ²⁶ Cartoon representations of the Au NPs at the high- and low-ligand densities are presented in Figure 2a,b and 2c,d, respectively. The resulting MM-

functionalized Au NPs were then employed for the NMR experiments.

2.3. Nuclear Magnetic Resonance Experiments. NMR spectra were obtained at 30 °C using a Bruker 800 MHz NMR spectrometer equipped with a ${}^{1}H/{}^{15}N/{}^{13}C$ cryoprobe with z-axis gradients. Data were acquired and processed using TopSpin 3.2 software and the software package Sparky (Goddard and Kneller, Sparky 3, University of California, San Francisco). Confirmation of the backbone assignments was guided using published chemical shift values (biological magnetic resonance data bank (BMRB) accession number 15514). Each sample had a constant protein concentration of 60 μ M in the NMR buffer (10 mM sodium acetate, pH 5.0, 10% D₂O, and 0.02% sodium azide). Representation of the MM-functionalized NPs employed for the NMR experiments is presented in Figure 2. NMR spectra were acquired at varying ratios of perdeuterated ¹⁵N-labeled F_C and MM-functionalized NPs (1:0.1-1:2). At higher amounts of NPs (1:>2), the NP-protein complex precipitated out of the solution, which could be due to a higher-order network formation in these systems. Control NMR experiments with hydroxyl linker-functionalized NPs and the F_C showed no changes in the combined chemical shift as a function of NP concentration, thus confirming the inert

nature of this hydroxyl backbone for our study (Figure S2). NMR experiments were also carried out with the labeled F_C and NPs in the presence of either 150 mM NaCl (high-density NPs) or 50 mM NaCl (low-density NPs) (note: comparison of results from DLS experiments of Au NPs in the presence of 150 or 50 mM NaCl with those obtained in the absence of salt confirmed the stability of NPs in salt solution (Figure S1a,b)). NP-induced changes in chemical shift were in fast exchange and at a population-weighted average of the unbound and bound chemical shifts. The changes in the combined chemical shift ($\Delta\delta_{\rm NH}$) upon ligand addition (NPs) were calculated using eq 1

$$\Delta \delta_{\rm NH} = \sqrt{(\Delta \delta_{\rm H})^2 + (0.2 \times \Delta \delta_{\rm N})^2}$$
 (1)

where $\delta_{\rm H}$ and $\delta_{\rm N}$ represent the change in the chemical shift of the amide proton and nitrogen, respectively. A weighting factor of 0.2 was employed to account for differences in the sensitivity of proton and nitrogen chemical shifts of the amide group. 16,46 The binding dissociation constant was calculated by fitting the changes in $^1{\rm H}$ and $^{15}{\rm N}$ chemical shifts as a function of ligand concentration using the N-site binding model, as described in eq 2

$$\Delta \delta_{\text{obs}} = \frac{(\Delta \delta_{\text{max}} \times [\text{NP}]_{\text{T}} \times N)}{K_{\text{D,app}} + ([\text{NP}]_{\text{T}} \times N)}$$
(2)

where $K_{\mathrm{D,app}}$ is the apparent binding dissociation constant, $[\mathrm{NP}]_{\mathrm{T}}$ is the total NP concentration used in the experiment, $\Delta \delta_{
m obs}$ is the observed change in chemical shift upon ligand addition, and N is the maximum number of binding sites. N was determined to be 26 based on the theoretical calculations for the total surface area of the F_C on a functionalized NP. Briefly, the dimensions of the side face of the F_C were determined using Molecular Operating Environment (MOE 2018, Chemical Computing Group) for calculating the total surface area for interactions with the NP surface, and the hydrodynamic radius of the NP systems as determined by DLS was used to calculate the total surface area on the NP for binding. Based on the $K_{\mathrm{D,app}}$ values, as well as the error in fitting, residues that were interacting with the ligands were identified and clustered into binding sites. Curve fitting and calculations were performed on Matlab R2019b, and the protein surface visualization was carried out on PyMol 2.3.5 viewer (Schrödinger).47

2.4. Protein Surface Properties. A structural model for the IgG1 F_C domain was built by homology modeling starting with the crystal structure for an aglycosylated human IgG1 F_C fragment (PDB code: 3S7G) using MOE. The electrostatic potential (EP) map was calculated at pH 5.0 using the adaptive Poisson–Boltzmann solver (APBS), ⁴⁸ and the surface aggregation propensity (SAP) map was generated as described by Chennamsetty et al. ⁴⁹ The resulting protein surface maps were then visualized using the PyMol 2.3.5 viewer (Schrödinger). ⁴⁷

2.5. Molecular Dynamics Simulations. 2.5.1. System Setup and Parameterization. Molecular dynamics simulations were performed using an IgG1 F_C domain molecule and MM ligandimmobilized SAM surfaces in explicit solvent. The F_{C} molecule was parameterized using the AMBER99^{50,51} force field, at pH 5.0, with a net charge of +15. SAM surfaces with immobilized Capto and Nuvia ligands were set up as described previously by our group. 52,53 SAM strands were built as alkyl thiol chains comprising 10 carbon atoms with one sulfur atom and a carbon atom at the base. Ligands were immobilized using a covalent bond between the base atom and the SAM alkyl chain. The sulfur atom at the base of the SAM strand and the seventh carbon from the sulfur were restrained with a harmonic potential of 40,000 kJ/mol·nm² to maintain the structure of the surface^{54,55} (note: Jamadagani et al. have used similar positional constraints on central atoms of the alkane chains to prevent deformation of the surface when simulating polymer folding and unfolding on SAM surfaces). The surfaces were constructed using an array of hydroxyl- or ligand-terminated SAM strands, with the hydroxyl-terminated strands providing a hydrophilic background to mimic a commercial resin matrix and the number of ligand-terminated SAM strands corresponding to the desired ligand density. Ligand head groups were parameterized using the general Amber force field⁵⁰

(GAFF), and charges were calculated with the AM1-BCC⁵⁷ approach. We note that aromatic interactions in this system are captured through this charge assignment process (no additional parameterization was performed). Hydroxyl group parameters were taken from a methanol-parameterized surface with the same force-field parameters. The position and orientation of the SAM strands were set to correspond to an alkyl thiol SAM immobilized on a (111) gold surface, as described by Love et al. ⁵⁸ We used a density of 1 ligand/nm² as high density and 0.3 ligand/nm² as low density to correspond to the commercial ligand densities of Capto MMC and Capto MMC ImpRes, respectively. TIP3P⁵⁹ water was used for all simulations, and Na+ ions were used to neutralize system net charge. Fifty nanosecond long simulations of isolated SAM surfaces (15 nm × 15 nm) were first performed independently, and the final SAM structure was used as the initial configuration for US simulations.

All simulations were performed using GROMACS⁶⁰ version 2019.4 in the NPT ensemble. The Nosé-Hoover⁶¹ thermostat and the Parrinello-Rahman⁶² barostat were used to maintain the temperature (298 K) and pressure (1 bar), respectively. Electrostatics were calculated using the particle-mesh Ewald method⁶³ with a grid spacing of 0.12 nm, fourth-order B-spline, and a direct sum tolerance of 10⁻³ (default parameters).

2.5.2. Umbrella Sampling (US) Simulations. Starting configurations for the umbrella sampling simulations were picked from constant velocity (± 0.01 nm/ps) pulling simulations, with the pull groups defined as the protein center of mass and the sulfur atoms at the base of the SAM, and the pulling reaction coordinate as the zdirection, in the NPT ensemble, with setup parameters as described above. A starting box size of 15 nm × 15 nm × 25 nm was consistently used for all simulations. To maintain the orientation of the protein, eight α carbons, two each in the C_H2 and C_H3 domains of the F_C molecule (Figure S3a), were restrained with a harmonic potential of 40 000 kJ/(mol·nm²) in the X and Y directions, as has been done previously.⁶⁴ The reaction coordinate for umbrella sampling was defined along the z-direction (z^*) between pull groups, protein center of mass and the carbons at the point of immobilization on the SAM (Figure S3b), and an umbrella potential of 0.5K (z $z_{\rm ref}$)² with $K = 1000 \text{ kJ/(mol \cdot nm}^2)$. The windows were selected such that the reaction coordinate $z_{\rm ref}$ for each window incremented by 0.1 nm, resulting in 95 windows for each system. Each of the window simulations was again performed in the NPT ensemble, with the same position restraints on the SAM strands and the protein as mentioned above. Production runs were 100 ns long, saving coordinates every 2 ps. The first 5 ns of production was discarded as equilibration for all simulations. The biased z^* distributions were stitched together to obtain the potential of mean force (PMF) curves using the WHAM 65,66 (weighted histogram analysis method), as made publicly available in the GROMACS wham utility.⁶⁷ VMD⁶⁸ was used for visualization of protein structures and MD simulation results.

3. RESULTS AND DISCUSSION

While it would be ideal to employ chromatographic resin beads for studying interactions with the F_C, the settling of micronsized resins makes it difficult to use them for the NMR experiments. To overcome this, recent work in our lab employed 3 nm diameter MM-functionalized Au NPs that mimicked the chromatographic resin surface for evaluating the binding regions on the ¹⁵N-labeled ubiquitin using NMR spectroscopy.²⁶ In the current work, we extend this approach to a significantly larger and more complex protein, the IgG1 F_C domain. To overcome any curvature effects that could occur during binding of the F_C, we synthesized larger Au NPs that were then functionalized with SAMs presenting MM ligand head groups representative of the commercial Capto MMC and Nuvia cPrime resin materials. Schematics of the NPs at low- and high-ligand densities for the "Capto ligand" and "Nuvia ligand" systems are presented in Figure 2a-d (note: while the Nuvia ligand was the same as employed in the

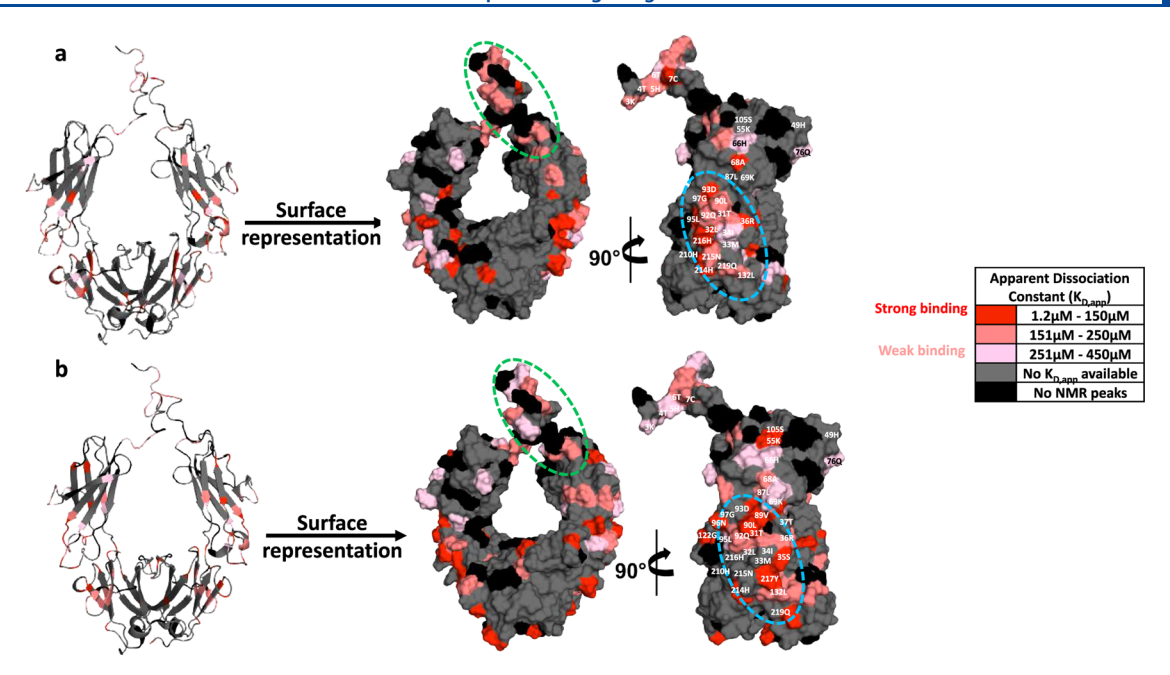


Figure 3. (a) "Capto ligand" high and (b) "Nuvia ligand" high NP binding sites on F_C domain as determined by NMR with color-coded apparent dissociation constant ($K_{D,app}$) for noninteracting (gray), strong (red), intermediate (salmon), and weak (pink) binding residues. Residues located in the hinge and C_H2-C_H3 interface regions are highlighted in green and blue ellipses, respectively. Unassigned residues and residues that were not visible in the spectrum due to concentration limitations are colored in black.

commercial resin, the Capto ligand was not an exact match to the chromatographic resin, missing the hydrophilic linker and the thio-ether group on "Capto ligand" NPs). Since only the ligand headgroup is responsible for interaction with the protein, ^{37,39} we believe that both NP ligand systems will provide important insights into the effects of ligand chemistry and density on protein binding. Further, recent work in our lab has shown differences in the binding thermodynamics of mAbs with Capto MMC and Capto MMC ImpRes resins (the two resins present the same functional headgroup at different ligand densities, ~1 and 0.3 ligand/nm², respectively). ⁶⁹ To further investigate these effects, the NPs were synthesized at high- and low-ligand densities, ~1 and 0.3 ligand/nm², respectively, for both "Capto ligand" and "Nuvia ligand" systems.

3.1. Gold Nanoparticle Synthesis and Functionalization with MM Linkers. As described in the Materials and Methods section and shown in Scheme 1, Au NPs were synthesized using a two-phase approach. The first phase included the generation of seed particles followed by increasing the size of the NPs in an aqueous growth solution. This was followed by the second phase, which involved transferring the NPs to an organic phase where they were functionalized with the MM linkers. Once functionalized, the NPs were precipitated and resolubilized in the NMR buffer. While initial efforts with the precipitation and resolubilization steps had several challenges due to irreversible aggregation of the NPs, we found that the addition of higher volumes of hexane (>5x volume of DCM) in concert with shorter centrifugation times (<2 min) and lower speeds (<1500 RCF) was successful in overcoming these issues and produced monodisperse MMfunctionalized Au NPs that were readily suspended at high concentrations in the NMR buffer.

The morphology of the functionalized NPs was then determined by TEM imaging, and the gold core size was measured using image j software. Figure 1a,b shows

representative TEM images of the "Nuvia ligand" high-density NPs and the corresponding gold core frequency distribution, respectively. As can be seen in the figures, the Au NPs were spherical in nature and the average gold diameter was calculated to be 5.9 ± 0.5 nm using image j software. The hydrodynamic radius of the functionalized NPs was measured to be 7 ± 0.5 nm with a polydispersity index of 0.18 using DLS (Figure S1a). The resulting NPs were then employed in the NMR titration experiments with the labeled F_C .

3.2. NMR Chemical Shift Perturbation Experiments. The binding of the MM-functionalized NPs to the $F_{\rm C}$ in solution was evaluated using NMR spectroscopy with a perdeuterated ¹⁵N-labeled $F_{\rm C}$. As described in the Materials and Methods section, MM ligand-functionalized NPs were titrated against a fixed concentration of the labeled $F_{\rm C}$ and the binding was monitored via the resulting ¹⁵N-TROSY spectra. In the NMR spectra, amide groups on the ¹⁵N-labeled amide backbone of the $F_{\rm C}$ that came into close proximity of the ligands experienced a change in the local electronic environment resulting in CSPs. In the resulting ¹⁵N-TROSY spectra, a single resonance peak was observed for both the unbound and bound states of the protein for each amide group. Thus, the observed peak was a population-weighted average of the two states and is defined by eq 3

$$\delta_{\text{obs}} = f_{\text{u}} \delta_{\text{u}} + f_{\text{h}} \delta_{\text{b}} \tag{3}$$

where $f_{\rm u}$ and $f_{\rm b}$ are the fractions of the unbound and bound proteins, respectively, and $\delta_{\rm u}$ and $\delta_{\rm b}$ are the chemical shift values of the unbound and bound states of the protein. Equations 2 and 3 were used to calculate the changes in the combined chemical shift as a function of NP concentration. When the NPs were first added to the $F_{\rm C}$ solution, a large fraction of the NPs would be expected to be in the bound state since the protein was in excess. As the titrations progressed, the concentration of the NPs increased, leading to the majority of the protein being in the bound state.

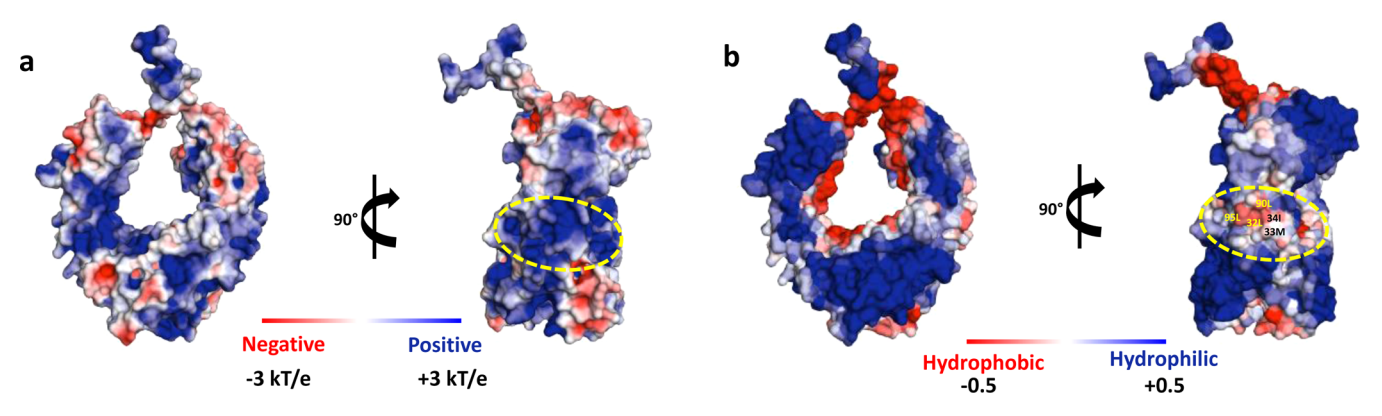


Figure 4. (a) Electrostatic potential (EP) map at pH 5.0 and (b) surface aggregation propensity (SAP) map of the F_C domain.

The assignments for F_C were available at 30 °C, and accordingly, the NMR experiments were carried out at this temperature. Since the temperature was sufficiently high, the line widths were observed to be free of exchange broadening and had ligand-dependent chemical shift values. Further, even though the molecular size of the F_C –NP complex was quite large, this temperature resulted in sufficiently fast tumbling to produce sharper spectra. As described in the Materials and Methods section, at higher NP-to-protein ratios, network formation of the complexes occurred, resulting in exchange broadening and eventually complete loss of the NMR signal at those conditions.

NMR experiments were performed with ¹⁵N-labeled F_C and "Capto ligand"- and "Nuvia ligand"-functionalized NPs at both high- and low-ligand densities. The CSP data at different NP concentrations for all F_C residues were analyzed using the method described previously.⁴³ Briefly, residues that exhibited linear migration trajectories with saturation behavior were fit to the N-site binding model, as described in eq 2. As described in the Materials and Methods section, a geometric analysis was carried out to estimate the maximum number of Fc molecules that could bind to a single NP, assuming that the side face of the F_C was the primary interacting binding region, as has been reported previously by our group. ⁴³ The results of this analysis indicated that there were at most 26 (N) binding sites (note: this calculation assumed that multiple ligand head groups could interact with a single residue/cluster of residues on the F_C surface). The total number of binding sites in each experiment was then determined and employed in concert with the CSP data at different NP concentrations to estimate the $K_{D,app}$ for all F_C residues using eq 2. A representative list of the $K_{D,app}$ and associated fitting error for all F_C residues that interacted with the high-density "Nuvia ligand" NP system are shown in Table S1.

3.2.1. Interactions of F_C with the High-Ligand Density Capto and Nuvia NP Systems. NMR experiments were carried out with the high-ligand-density "Capto ligand" and "Nuvia ligand" NP systems, and F_C residues that exhibited saturation behavior for interactions with the NPs were color-coded based on their $K_{D,\mathrm{app}}$ values, and the resulting projections on the protein surface are presented in Figure 3a,b, respectively. As can be seen in the figure, the $K_{D,\mathrm{app}}$ values are presented in a color scale ranging from red to pink, with residues that did not exhibit significant CSPs indicated in gray. Residues for which the NMR data were not available are shown in black. To facilitate the discussion, both the cartoon and surface representations of the protein surface are presented

in the figure. As can be seen, the μ M $K_{D,app}$ values obtained from NMR experiments with the NPs (Figure 3) were 3 orders of magnitude smaller than those obtained previously with these ligands in solution. These results clearly indicate enhanced binding of the F_C to MM-functionalized surfaces. As discussed in our work with ubiquitin binding to NP surfaces, this enhanced affinity is likely due to a combination of avidity (multipoint attachment) and cooperativity (synergistic interactions) effects.

As can be seen in Figure 3, the majority of the residues involved in binding were located either in the hinge region (green ellipse) or near the interface of the C_H2 and C_H3 domains (blue ellipse). For the "Capto ligand" high NPs (Figure 3a), residues on the F_C with the strongest interactions were located near the interface of the C_H2 and C_H3 domains and were observed to be either aliphatic (e.g., 95L, 32L, 90L) or positively charged (e.g., 214H, 216H, 36R). The other residues that interacted in the interface region included a combination of aliphatic (e.g., 90L, 34I, and 33M) and polar residues (e.g., 97G, 31T, 92Q, 215N, and 219Q). A negatively charged residue 93D also exhibited NMR shifts, which may be due to its proximity to the interacting residues indicated above. While the results with the "Nuvia ligand" high NPs (Figure 3b) indicated similar binding regions to that observed with the Capto high NPs, the Nuvia results were more widely distributed on the F_C surface. Further, the contiguous binding region at the interface of the C_H2 and C_H3 domains (blue ellipse) contained strongly binding aliphatic (e.g., 90L, 89V), polar (96N, 122G, 31T, 35S, and 219Q), and positively charged (e.g., 214H and 69K) residues. Thus, while the binding regions were similar with the two NPs, there were subtle differences in their interactions with the F_C.

3.2.1.1. Comparison of NMR Results with Protein Surface Property Maps. To investigate these binding regions in more detail, the NMR results were compared with EP and SAP surface property maps of the F_C at pH 5. As can be seen in the EP map (Figure 4a), a large region of positive electrostatic potential is present on the side face of the F_C , which corresponded with a number of positively charged residues (e.g., 214H, 210H, 36R, 69K, 82R, and 91H) that exhibited strong interactions with the "Nuvia ligand" high NPs (Figure 3b). In contrast, the results with the "Capto ligand" high NP system (Figure 3a) were less correlated with this large region of positive EP. These results suggest that even though similar binding regions were identified for F_C interactions with the two MM NPs, the binding to the Nuvia high NPs was more electrostatically driven.

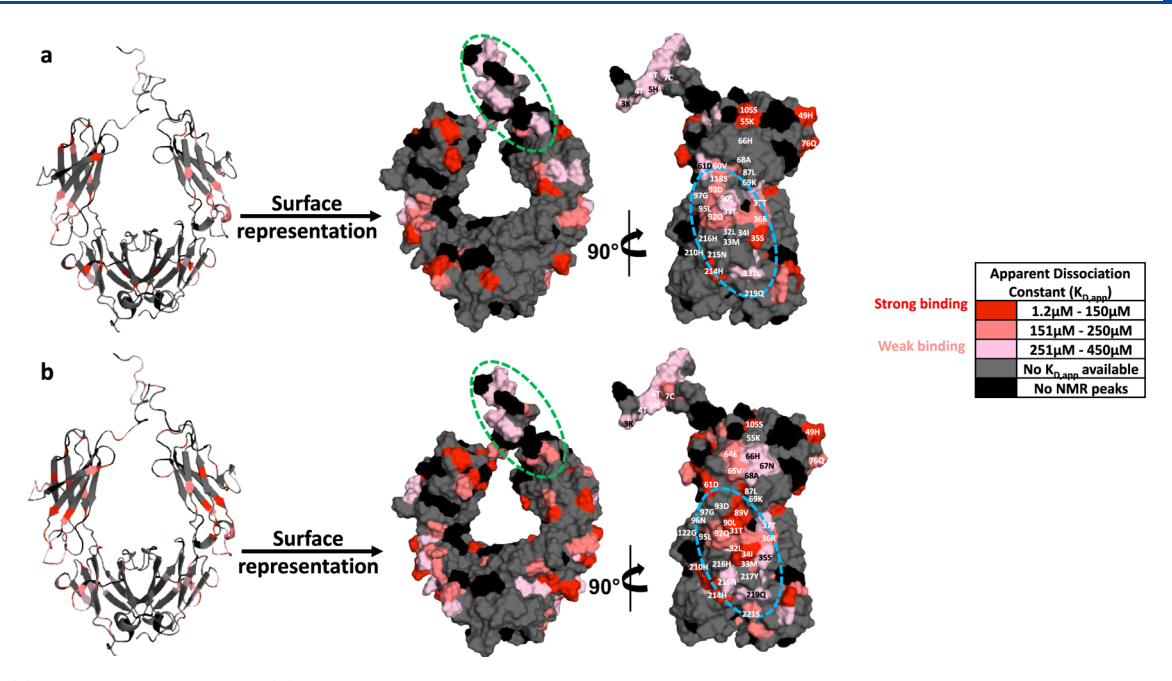


Figure 5. (a) "Capto ligand" low and (b) "Nuvia ligand" low NP binding sites on F_C domain as determined by NMR, with color-coded apparent dissociation constants (K_{D} , app) for noninteracting (gray), strong (red), intermediate (salmon), and weak (pink) binding residues. Residues located in the hinge and CH2–CH3 interface regions are highlighted in green and blue ellipses, respectively. Unassigned residues and residues that were not visible in the spectrum due to concentration limitations are colored in black.

As can be seen in the SAP map (Figure 4b), a number of adjacent aliphatic residues (95L, 32L, 90L, 34I, 33M, and 160V) in the interface of the C_H2 and C_H3 domains formed a strong hydrophobic region on the surface of the protein (indicated by a yellow ellipse). Interestingly, while all of these residues interacted with relatively high binding affinities to the "Capto ligand" high NPs (Figure 3a), only the 90L exhibited a strong interaction with the "Nuvia ligand" system (Figure 3b). In fact, the Fc binding region to the "Capto ligand" high NPs (Figure 3a) corresponds quite well with the indicated region on the SAP map (yellow ellipse in Figure 4b), indicating that hydrophobic interactions, primarily involving aliphatic residues, were major drivers in the "Capto ligand" system. Further, this relatively small binding region also overlaps with the strong positive electrostatic potential (yellow ellipse in Figure 4a), indicating that synergistic interactions may also be important.

3.2.2. Interactions of F_C with the Low-Ligand Density Capto and Nuvia NP Systems. Ligand density has been shown to have an important impact on the behavior of MM chromatographic systems. 9,38,69 Further, recent simulation work in our group has shown that the Capto ligand at sufficiently high-ligand surface densities tends to self-associate, resulting in the formation of hydrophobic clusters on the surface. 44 Importantly, this behavior did not occur in simulations at lower "Capto ligand" densities or with "Nuvia ligand"-functionalized surfaces. The formation of ligand clusters can, in turn, impact the hydrophobic length scale, which has been shown to have a significant impact on hydrophobicity. To investigate the impact of ligand density on F_C interactions, we synthesized MM-functionalized Au NPs at low-ligand density (~0.3 ligand/nm²). NMR experiments were then performed with labeled F_C and the lowdensity "Capto ligand" and "Nuvia ligand" NPs, and the CSP data were fit to the N-site binding model to determine the residue-specific $K_{D,app}$. The F_C residues that exhibited

measurable $K_{D,app}$ values for interactions with "Capto ligand" low and "Nuvia ligand" low NPs were then depicted on the protein surface using an appropriate color scheme, and the results are presented in Figure 5.

3.2.2.1. NMR Result Comparison for High- and Low-Ligand Density Capto NP Systems. As can be seen in the figure, the F_C interacted with lower affinity to the low-density MM NPs as compared to the high-density systems (Figure 3). For the "Capto ligand" system, while many of the important interacting residues were similar at both ligand densities, some of the interacting residues were observed to be different. For example, the cluster of aliphatic residues (32L, 33M, and 34I) in the interface of the C_H2 and C_H3 domains that interacted weakly with the "Capto ligand" high NPs did not exhibit any measurable interactions with the Capto low NPs. On the other hand, some positively charged residues (e.g., 55K, 49H) near the hinge region exhibited an increase in binding affinity on the low-density system (Figure 5a) as compared to the "Capto ligand" high NPs (Figure 3a). These results show how liganddensity variation can impact not only the overall binding affinity but also the important interaction sites on protein surfaces in MM CEX systems. These differences in interaction sites can potentially play an important role in the separation of target products from challenging protein mixtures (e.g., removing product-related variants).

3.2.2.2. NMR Result Comparison for High- and Low-Ligand Density Nuvia NP Systems. In contrast to interactions of the Fc with the "Capto ligand" low NPs, the "Nuvia ligand" low NP system (Figure 5b) did not show significant differences in interacting residues as compared to the "Nuvia ligand" high-density NPs (Figure 3b). Further, as observed for the high-density "Nuvia ligand" NPs, the low-density results also indicated that the binding regions were well correlated with the positive EP surface on the side face of the F_C. Interestingly, while the Fc binding to the "Nuvia ligand" NPs appeared to be strongly influenced by electrostatic interactions, both the

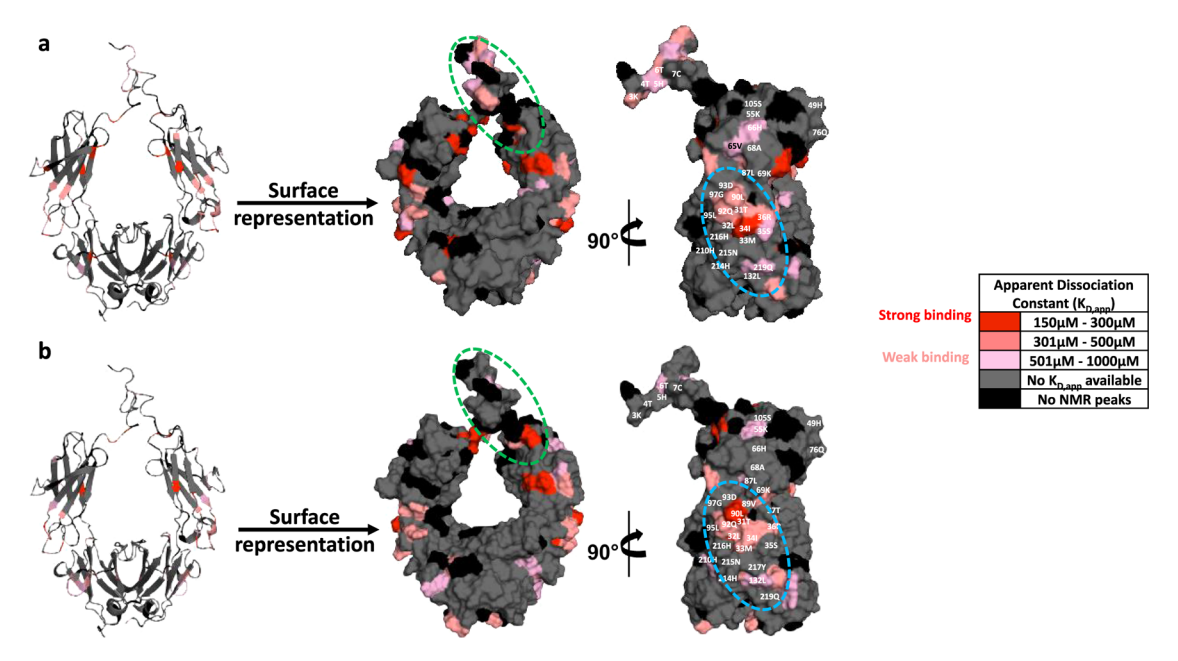


Figure 6. (a) "Capto ligand" high and (b) "Nuvia ligand" high NP binding sites on F_C domain in the presence of 150 mM NaCl as determined by NMR, with color-coded apparent dissociation constants ($K_{D,app}$) for noninteracting (gray), strong (red), intermediate (salmon), and weak (pink) binding residues. Residues located in the hinge region and in the interface of the C_H^2 and C_H^3 domains are highlighted in green and blue ellipses, respectively (note the difference in the magnitude of the color scale as compared to Figure 3). Unassigned residues and residues that were not visible in the spectrum due to concentration limitations are colored in black.

aliphatic residues 89V and 90L exhibited strong binding affinities at low- and high-ligand densities, indicating that hydrophobic and/or synergistic interactions also played a contributing role. To further investigate the relative contributions of charge and hydrophobicity in binding in these systems, we performed NMR experiments with the MM-functionalized NPs and labeled $F_{\rm C}$ in the presence of NaCl.

3.2.3. Interactions of F_C with the High-Density Capto and Nuvia NPs in the Presence of Salt. NMR experiments were carried out with labeled F_C and the high-density NPs in the presence of 150 mM sodium chloride. Again, the CSP data at different NP concentrations were fit to the N-site binding model and the residue-level $K_{D,\rm app}$ values were determined. F_C residues that showed measurable $K_{D,\rm app}$ were then color-coded based on their strength of binding, and the resulting projections on the protein surface are presented in Figure 6.

3.2.3.1. Comparison of F_C -Interacting Residues with the High-Density Capto NP System in the Presence and Absence of Salt. As can be seen in the figure, interactions of F_C with the high-density MM-functionalized NPs became weaker in the presence of 150 mM NaCl, as indicated by the increase in the $K_{D,app}$ values (note: a different color scale was employed in Figures 3 and 6). For the "Capto ligand" high NPs (Figure 6a), residues on the F_C with the strongest interactions were localized around the group of aliphatic residues (32L and 34I) in the interface of the C_H2 and C_H3 domains (blue ellipse). Other residues that interacted in this region included a combination of aliphatic (e.g., 90L), polar (e.g., 97G, 92Q, 31T, and 35S), and positively (e.g., 36R) charged residues. Interestingly, interactions with positively charged residues (e.g., 214H, 210H, and 216H) in this region that were important at no salt (Figure 3a) were now screened at the 150 mM conditions (Figure 6a). In contrast, residue 34I that showed weak interactions with the "Capto ligand" high-density NPs in the buffer (Figure 3a) interacted relatively strongly in the presence of salt. On comparing these NMR results with the "Capto ligand" high NPs with the protein SAP map (yellow ellipse in Figure 4b), it becomes clear that interactions with the hydrophobic residues on the $F_{\rm C}$ surface became even more important in the presence of NaCl. These observations are in line with the expectation that the presence of high amounts of salt would result in the screening of electrostatics while increasing the hydrophobic interactions.

3.2.3.2. Comparison of F_C -Interacting Residues with the High-Density Nuvia NP System in the Presence and Absence of Salt. The results with the "Nuvia ligand" high NPs in the presence of 150 mM salt (Figure 6b) were quite different from those obtained at no salt conditions (Figure 3b). As can be seen in the figures, in the hinge region (green circle), a dramatic decrease in the number of interacting residues was observed at the higher salt condition. This can also be seen when examining the side face of the F_C, where interactions with the positively charged (e.g., 3K, 5H, and 66H) residues were screened and residue 55K exhibited a decrease in affinity at the high salt. This impact of salt was also observed for interactions of the residues in the interface of the C_H2 and C_H3 domains (blue ellipse). Interactions with most of the positively charged (e.g., 214H, 69K) and polar (e.g., 122G, 96N, 219Q, and 35S) residues in this region were screened in the presence of salt. On the other hand, a cluster of aliphatic residues (e.g., 32L, 34I, 33M, 95L, and 90L) still exhibited interactions with the "Nuvia ligand" high NPs at 150 mM NaCl, albeit with lower affinities. These results indicate that while electrostatic interactions decreased, most of the hydrophobic interactions remained for the binding of F_C with the "Nuvia ligand" high NPs at higher salt. The observed binding region at the interface of the $C_{\rm H}2$ and $C_{\rm H}3$ domains with both MM NPs was similar at the high salt condition, in sharp contrast to the results at the lower salt condition.

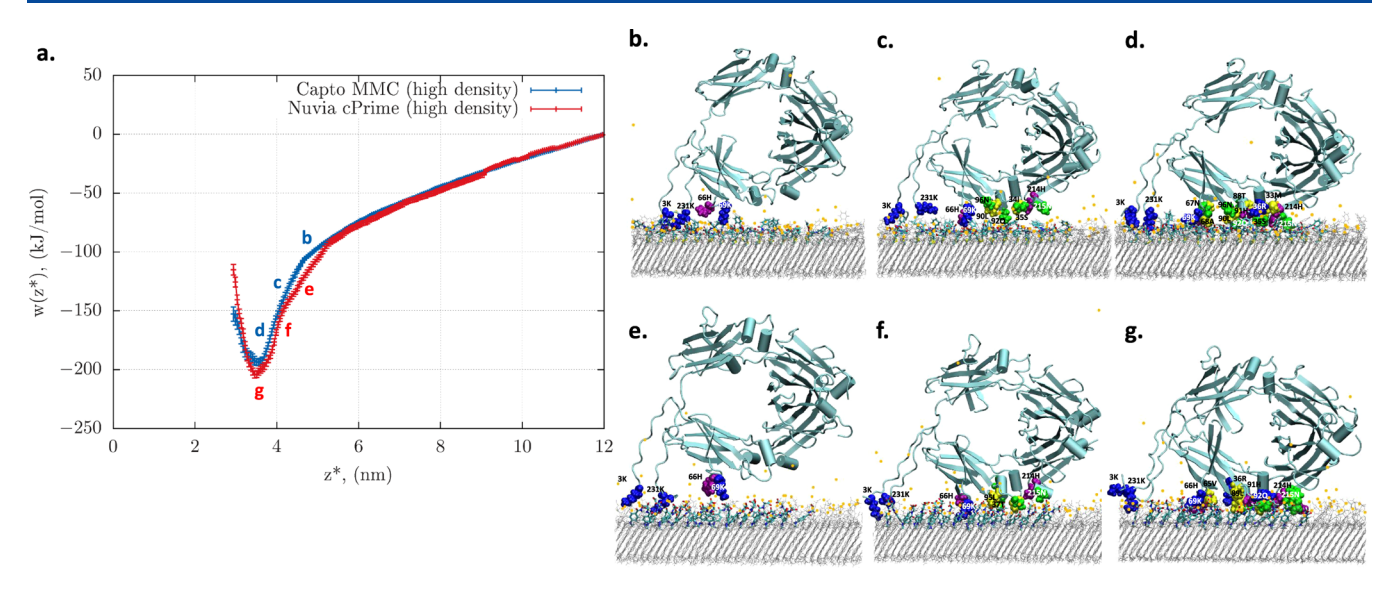


Figure 7. Molecular dynamics (MD) simulation-based investigation of protein—high-density SAM binding. (Left) (a) "Capto ligand" SAM $-F_C$ PMF (blue) and "Nuvia ligand" SAM $-F_C$ PMF (red) for the "preferred" face interacting with this surface. (Right) (b-g) Representative structures of F_C 's "preferred" face bound to the SAM at different separation distances (color coding for parts (b)-(g): SAM shown in gray sticks, ligand head groups in licorice, sodium counterions in orange spheres, protein backbone as a cyan cartoon, positively charged side chains involved in binding in blue, negatively charged in red, polar in green, nonpolar in yellow, positive histidines in purple).

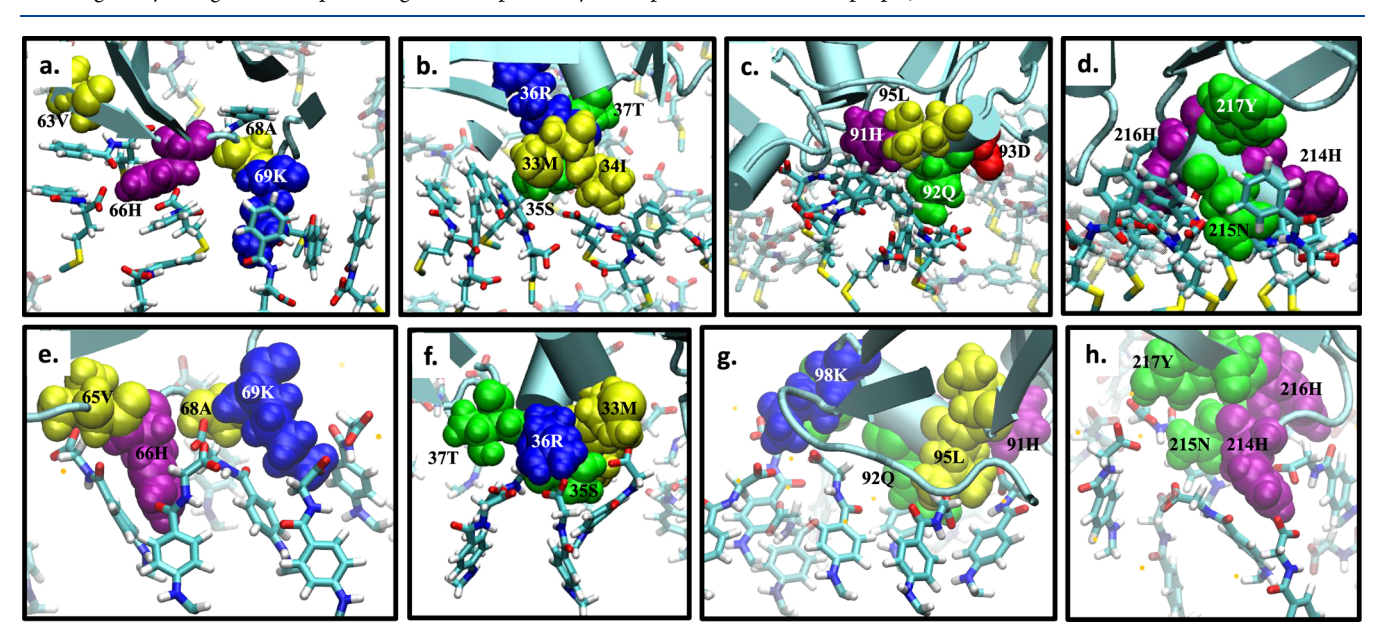


Figure 8. Representative structures of different F_C surface residues bound to Capto MMC (a-d) and Nuvia cPrime (e-h) ligands on a high-density SAM surface (color coding: ligand head groups in licorice representation, sodium counterions in orange spheres, protein backbone as a cyan cartoon, positively charged side chains involved in binding in blue, negatively charged in red, polar in green, nonpolar in yellow, positive histidines in purple).

NMR experiments were carried out with the high-density NPs at 300 mM NaCl, and similar residues were shown to be involved in binding with the $F_{\rm C}$, albeit at lower affinities (high $\mu{\rm M}$ to low mM) (results not shown). In addition, we attempted to conduct the NMR experiments at 150 mM NaCl with the low-density MM NPs; however, the data from these experiments indicated no measurable interactions of the $F_{\rm C}$ with these NPs.

We also examined the impact of salt on the EP surface map of the F_C and found that there was minimal impact on the surface potential at 150 mM NaCl. Interestingly, the overlapping region of hydrophobicity and positive EP

indicated by the yellow ellipse in the protein surface property maps (Figure 4) was found from the NMR to be the common interaction region with both high-density MM NPs in the presence of salt. This observation is intriguing and indicates that at elevated salt, it may be necessary to have both electrostatic and hydrophobic interactions occurring on a preferred binding region of the protein to have these salt-tolerant interactions.

3.3. Molecular Dynamics Simulations. 3.3.1. Interactions with High-Density SAMs. To further investigate the molecular-level interactions and to explore the bound conformations of the F_C to these surfaces, umbrella sampling

(US) simulations were carried out with the experimentally determined binding hotspot oriented toward the SAM surfaces. Since these biased MD simulations focus on the interactions of specific orientation of the F_C molecule with the ligand surface, a direct comparison to the NMR results cannot be made. However, these simulations can be used to gain further insight into the adsorption behavior and likely intermolecular interactions between the C_H2/C_H3 interface of the F_C and the ligand-immobilized SAM surfaces. Potentials of mean force (PMF) and $w(z^*)$ were calculated from these simulations, and the results for the high-ligand-density SAM surfaces are shown in Figure 7a. As can be seen in the figure, the PMFs for both the Capto and Nuvia systems had similar shapes, with the $w(z^*)$ minima occurring at $z^* \sim 3.51$ nm and $z^* \sim 3.46$ nm, respectively (note: z^* corresponds to the distance from the center of mass of the F_C to the point of ligand immobilization on the SAM surface). The depths of the PMF minima obtained in these simulations indicated similar free energy of adsorption of the F_C to both the "Capto ligand" and the "Nuvia ligand" SAM surface.

Figure 7 also presents snapshots of the F_C molecule as it approached the SAM surface at discrete z^* locations. For F_C binding to both "Capto ligand" and "Nuvia ligand" surfaces, only positively charged (e.g., 3K, 66H, 69K) residues were seen to interact at longer distances (Figure 7b,e). As the F_C was sampled closer to the ligand-coated SAM surfaces, positions c and f (Figure 7), polar (e.g., 37T, 92Q, 96N), and aliphatic (e.g., 34I, 35S, 90L, 95L) residues were then observed to interact with the "Capto ligand" and "Nuvia ligand". At even shorter distances (Figure 7d,g), additional aliphatic (e.g., 68A, 89L) and positively charged (e.g., 36R, 214H) residues were found to interact with the ligand surfaces. It is important to note that the residues observed to interact in the MD simulations for both surfaces at the PMF minimum were similar to those identified from the NMR experiments (Figure 3). These results with the F_C show a similar trend as was observed in previous work with ubiquitin, 64 where longrange electrostatic attractions initially brought the protein closer to the ligand surface and a combination of electrostatic and short-ranged hydrophobic interactions resulted in strong binding at the minimum.

To investigate residue—ligand interactions in more detail, contact statistics (averaged over simulation trajectory) for heavy atoms of F_C residues and MM ligands on the SAM (cutoff = 3Å) were obtained at the PMF minima (Table S2). MD trajectories were examined further to obtain representative snapshots (Figure 8) of residues with high contact frequencies. In this figure, we compare several groups of residues at the binding interface and their interactions with the ligands on the "Capto ligand" and "Nuvia ligand" surfaces.

Our group has recently demonstrated the phenomenon of self-association in ligand-immobilized SAM surfaces, where the solvent-exposed aromatic moieties on the "Capto ligand" high-density surface were observed to aggregate and form hydrophobic clusters. ⁴⁴ This was markedly different from the low-density system, where the ligands were separated by large enough spacings to prevent interactions with neighboring ligands resulting in a nonclustered surface. For the "Nuvia ligand" surface, the buried aromatic moiety and reduced flexibility around the point of immobilization prevented ligand self-association.

As can be seen, in these various snapshots (Figure 8), we again observed ligand self-association on the "Capto ligand"

high-density surface, even in the presence of the protein. These ligand clusters played an important role in the interactions with the $F_{\rm C}$. In contrast, no ligand clusters were observed with the "Nuvia ligand" surface and all interactions of residues on the FC were with individual ligands.

Figure 8a,e shows a snapshot of a group of residues on the F_C interacting with the "Capto ligand" and "Nuvia ligand" surfaces, respectively. For the "Capto ligand" SAM, the aliphatic (63V) and the adjacent positively charged residues (66H, 69K) on the F_C were each directly involved in interactions with a cluster of "Capto ligands". While 66H appeared to interact via both $\pi-\pi$ and electrostatic interactions, 69K interacted primarily with the carboxyl moiety. For the "Nuvia ligand" SAM, no clustering was observed for the ligands interacting with this group of F_C residues (Figure 8e) and interactions with the ligand surface were electrostatically driven (e.g., 66H, 69K) due to solvent-exposed carboxylate groups on the Nuvia ligands.

As shown in Figure 8b, a group of aliphatic and polar residues (e.g., 33M, 34I, 37T, and 35S) in the $C_{\rm H}2/C_{\rm H}3$ interface of the $F_{\rm C}$ was observed to interact with clusters of "Capto ligands". The aliphatic residues in this group had fewer interactions (Table S2) with the "Nuvia ligand" surface (Figure 8f), a result that was qualitatively similar to that observed in the NMR results (Figure 3). As can be seen in Figure 8f, the positively charged residue 36R was responsible for electrostatic interactions with the carboxyl moieties on the "Nuvia ligand" surface, with the aliphatic residues pointing away from the ligand SAM. Thus, for this group of residues on the $F_{\rm C}$ surface, there was a marked difference in the behavior with the two MM SAM surfaces.

Another group of residues at the $C_{\rm H}2/C_{\rm H}3$ interface (Figure 8c,g) had marked differences in the modes of interaction with the "Capto ligand" and "Nuvia ligand" SAMs. A group of charged (91H), polar (92Q), and aliphatic (95L) residues had significant, multiple points of interaction with a cluster of "Capto ligands". In contrast, for the "Nuvia ligand" system, these residues were seen to interact with individual nonclustered ligands. Interestingly, the negatively charged residue, 93D, which was observed to have a significant NMR shift in the high-density Capto experiment (Figure 3), was observed in the simulations to be adjacent to the interacting residues on the Capto SAM but not directly involved in any interactions with the ligands. Thus, this residue's NMR shift was likely due to its proximity rather than direct interaction with the ligand surface.

Figure 8d shows a snapshot of the F_C surface patches 214H, 215N, and 216H interacting with another "Capto ligand" cluster. The histidine residues were seen to interact via both π – π stacking and electrostatic interactions, an observation that has also been seen in recent simulations from our group with F_C and MM ligands in free solution. All three residues had multiple interactions with the ligands in this cluster on the SAM, likely resulting in synergistic interactions. In contrast, for the "Nuvia ligand" SAM, these residues interacted with individual nonclustering ligands. When comparing these results to the NMR experiments, it is interesting to note that while residues 214H, 215N, and 216H were seen to have significant NMR shifts with the "Capto ligand" SAM, only 214H had measurable NMR shifts with the "Nuvia ligand" SAM.

3.3.2. Interactions with Low-Density SAMs. To investigate the effects of ligand density on F_C binding and interacting residues, US simulations were also performed with these MM

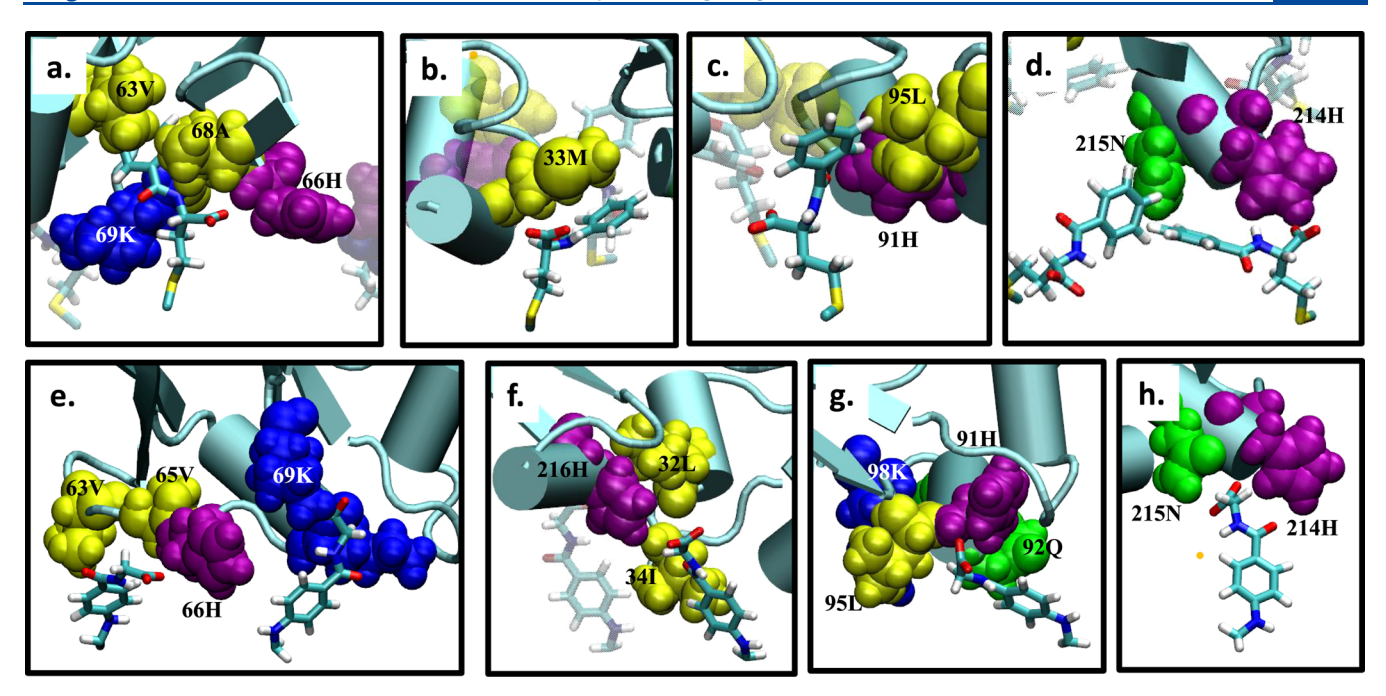


Figure 9. Representative structures of different F_C surface residues bound to Capto MMC ligands (a-d) and Nuvia cPrime ligands (e-h) on low-density SAM surfaces (color coding: ligand head groups in licorice representation, sodium counterions in orange spheres, protein backbone as a cyan cartoon, positively charged side chains involved in binding in blue, negatively charged in red, polar in green, nonpolar in yellow, positive histidines in purple).

ligands immobilized at a lower-ligand density. The ligand immobilization on the two SAM surfaces at this density was too sparse for any clustering to occur in the case of either ligand, as reported previously by our group. 44 The PMF curves are compared in Figure S4, and the $w(z^*)$ minimum for the "Capto ligand" SAM was found to be only slightly less favorable than "Nuvia ligand" SAM. Figure S4 also presents snapshots of the F_C molecule as it approached the SAM surfaces at different values of z* for both "Capto ligand" (Figure S4b-d) and "Nuvia ligand" (Figure S4e-g). Similar to the high-density system, long-range electrostatic attractions between the SAM surfaces and the positively charged residues on the F_C surface brought the protein closer to the surface. At closer distances (lower values of z^*), this was followed by interactions between aliphatic and aromatic residues on the F_C and hydrophobic moieties on the ligands.

Residue-ligand interactions in these systems were examined as well, using snapshots from the US trajectories at the $w(z^*)$ minima (Figure 9). Ligand clustering was not observed at the low density, resulting in interactions of individual Capto and Nuvia ligands with multiple F_C residues over the course of the simulation. In contrast to the results with the high-density SAM, the interactions at the lower densities were quite similar with the "Capto ligand" and "Nuvia ligand" systems. Of more interest is a comparison between the low- and high-density SAMs for a given MM ligand. As shown in Figure 9a, a single "Capto ligand" was observed to interact with multiple residues, both aliphatic (68A) and positively charged (66H, 69K). This contrasts with the higher-density result (Figure 8a) where several clusters of ligands were seen to be interacting with this region of the protein. For the low-density Nuvia SAM, individual ligands interacted with both aliphatic (63V) and charged (66H) residues in this group via both van der Waals and electrostatic interactions (Figure 9e). In contrast, at the

high-ligand density, multiple ligands were seen to interact synergistically with these F_C residues (Figure 8e).

For another group of residues in this region, a comparison between the low- and high-density "Capto ligand" surfaces showed that while interactions were observed only between 33M and a single ligand at the low density (Figure 9b), clustering in the higher-density SAM resulted in a hydrophobic patch allowing for more interactions (Figure 8b). For the low-density "Nuvia ligand" SAM, individual ligands interacted with multiple different residues over time, both aliphatic (34I) and charged (216H) (Figure 9f). In contrast, at the higher-ligand density, multiple ligands interacted synergistically with these residues.

This trend of individual ligand interactions with the low-density SAM as compared to the ligand clustering and synergistic interactions with multiple ligands on the high-density SAM continued with the other grouping of residues at the interface region (Figures 9 and 8, parts c, d, g, and h). A comparison of the simulation and NMR results with low-density SAMs indicated a general agreement with the residues involved in binding in the interface region.

4. CONCLUSIONS

In this work, we developed a Au NP-based pseudo-solid-state system that mimicked different MM chromatographic systems and was amenable to NMR experiments with relatively large biomolecules such as the IgG1 $F_{\rm C}$ domain. NMR experiments were carried out with a $^{15}\text{N-labeled}$ $F_{\rm C}$ and various MM NPs to get insights into the effects of ligand chemistry and density on $F_{\rm C}$ binding, as well as the nature of interactions in these protein—ligand systems.

The results from the NMR experiments suggested that the binding of F_C to the MM-functionalized NPs resulted in stronger residue binding (μ M affinities) as compared to the mM binding observed with these ligands in free solution. The

higher binding affinity observed with the NPs could be due to a combination of cooperativity and avidity effects for the $F_{\rm C}$ binding in these systems. The binding of $F_{\rm C}$ with the "Capto ligand" high NPs was concentrated around a strong interacting hydrophobic aliphatic region (32L, 95L, and 90L) in the interface of the $C_{\rm H}2$ and $C_{\rm H}3$ domains, which also corresponded well with a focused hydrophobic region on the protein surface SAP map. In contradistinction, the relatively strong binding with the "Nuvia ligand" high NPs was observed to be more diffuse throughout the side face of the $F_{\rm C}$ and corresponded well with the contiguous positive EP region on this surface of the protein.

We also investigated the effect of ligand density on these binding interactions and observed a decrease in binding affinity for both NP systems at the lower densities. In addition, while many of the interacting residues were similar at the two ligand densities for the "Capto ligand" NP systems, several aliphatic residues (33M, 32L, and 34I) in the interface region that were important at the higher density did not interact with the Capto low NPs. This result shows how ligand density can not only affect the binding affinities but also impact the important interaction sites on the protein surface. In contrast, we did not observe any significant difference in the interacting residues in the high- and low-ligand-density "Nuvia ligand" NPs, with the binding region again correlating well with the EP map.

NMR experiments with the labeled F_C and MM-functionalized NPs were also carried out in the presence of salt. As expected, the binding affinities of F_C to both MM-functionalized NPs decreased in the presence of salt. For the "Capto ligand" NP system, the salt screened weak interactions of some of the polar and positively charged residues on the side face of the F_{C} resulting in an even more focused hydrophobic binding region in the interface of the C_H2 and C_H3 domains. This effect was even more pronounced on the "Nuvia ligand" surface where the presence of salt had a dramatic impact on the binding region, transitioning from a large diffuse region to a significantly smaller, focused hydrophobic region at the higher salt. These observations further support the contention that even though both ligands appeared to interact with regions of positive charge and hydrophobicity, the interactions of "Capto ligand" NPs were more hydrophobic in nature, while those with "Nuvia ligand" were more electrostatically driven. Interestingly, at higher salt, both MM NP systems exhibited the same focused binding region, which also corresponded to the overlapped SAP and EP regions determined from the protein surface property analysis. These results clearly demonstrate how salt can impact the relative contributions of electrostatic and hydrophobic interactions in these MM systems and how these effects can be different for various MM ligand chemistries, with potential implications for selectivity.

In addition, MD simulations were employed to obtain a molecular understanding of the ligand—ligand and ligand—residue interactions involved in F_C binding to MM ligand surfaces. US simulations (with the C_H2/C_H3 interface of the protein oriented toward the ligand SAM) were carried out to obtain PMF curves for Fc adsorption to both high- and low-density, "Capto ligand" and "Nuvia ligand" SAM surfaces. In general, for all systems, the binding of the protein was driven by long-range electrostatics at larger distances followed by varying degrees of hydrophobic and aliphatic interactions at shorter distances. MD trajectories at the PMF minimum were further investigated to isolate the residue—ligand interactions in the C_H2 and C_H3 interface region. For the high-density

ligand surfaces, we observed that ligand clustering on "Capto ligand" surface was responsible for subtle differences in the binding of residues to the ligand-coated SAM. In particular, several groups of polar and charged residues on the F_C were observed to interact with clusters of "Capto ligands", likely resulting in synergistic interactions. On the other hand, residue—ligand interactions on the high-density "Nuvia ligand" surface appeared to be primarily electrostatically driven, with individual nonclustering ligands. These results elucidate the significant impact of ligand self-association on protein adsorption since these differences in binding behavior can be attributed to the different relative contributions from hydrophobic and electrostatic interactions with clustering and nonclustering surfaces.

The biophysics/simulation approach presented in this paper provides a useful platform for examining large biomolecule—surface interactions at the molecular level. While this study focused on the binding of the $F_{\rm C}$ domain to MM systems, it can be readily applied to other protein—ligand systems. Future work will extend this work to other large biomolecules of industrial importance, as well as novel MM ligands and surfaces that may offer enhanced selectivity/orthogonality for challenging bioseparation problems.

ASSOCIATED CONTENT

Supporting Information

The Supporting Information is available free of charge at https://pubs.acs.org/doi/10.1021/acs.langmuir.1c02114.

DLS analysis of "Nuvia ligand" high-density NP size distribution in the absence and presence of 150 mM NaCl (Figure S1), ¹⁵N-TROSY NMR spectra of the F_C domain at varying concentrations of hydroxyl linkerfunctionalized Au NPs (Figure S2), backbone residues of the F_C molecule, where α carbons were restrained to maintain the protein orientation and schematic representation of the reaction coordinate used for umbrella sampling (Figure S3), MD simulation-based investigation of protein—low-density SAM binding (Figure S4); a list of residues on the F_C surface interacting with the high-density "Nuvia ligand" NP system in the absence (no salt) and presence of 150 mM NaCl (Table S1), and scaled contact frequency values for some key residues for four different trajectories at PMF minima (Table S2) (PDF)

AUTHOR INFORMATION

Corresponding Author

Steven M. Cramer — Howard P. Isermann Department of Chemical and Biological Engineering and Center for Biotechnology and Interdisciplinary Studies, Rensselaer Polytechnic Institute, Troy, New York 12180, United States; orcid.org/0000-0003-4993-0826; Email: crames@rpi.edu

Authors

Ronak B. Gudhka — Howard P. Isermann Department of Chemical and Biological Engineering and Center for Biotechnology and Interdisciplinary Studies, Rensselaer Polytechnic Institute, Troy, New York 12180, United States; Present Address: Scientist, Process Development, Amgen Inc., Cambridge, Massachusetts 02141, United States; orcid.org/0000-0001-8959-6485

- Mayank Vats Howard P. Isermann Department of Chemical and Biological Engineering and Center for Biotechnology and Interdisciplinary Studies, Rensselaer Polytechnic Institute, Troy, New York 12180, United States; orcid.org/0000-0003-4040-2090
- Camille L. Bilodeau Howard P. Isermann Department of Chemical and Biological Engineering and Center for Biotechnology and Interdisciplinary Studies, Rensselaer Polytechnic Institute, Troy, New York 12180, United States; Present Address: Postdoctoral Researcher, Massachusetts Institute of Technology, Cambridge, Massachusetts 02139, United States.; oorcid.org/0000-0002-8358-5280
- Scott A. McCallum Center for Biotechnology and Interdisciplinary Studies, Rensselaer Polytechnic Institute, Troy, New York 12180, United States
- Mark A. McCoy Mass Spectrometry & Biophysics, Merck & Co., Inc., Kenilworth, New Jersey 07033, United States; orcid.org/0000-0003-3994-6605
- David J. Roush Biologics Process R&D, Downstream
 Purification Development and Engineering, Merck & Co.,
 Inc., Kenilworth, New Jersey 07033, United States

 Mark A. Snyder Process Chemistry Division, Bio-Rad
 Laboratories, Hercules, California 94547, United States

Complete contact information is available at: https://pubs.acs.org/10.1021/acs.langmuir.1c02114

Notes

The authors declare no competing financial interest.

■ ACKNOWLEDGMENTS

This work was supported by the National Science Foundation (Grant number CBET 1704745), as well as Merck & Co., Inc. (Kenilworth, NJ) and Bio-Rad Laboratories (Hercules, CA). High-Performance Computing resources for simulations were provided by the Center for Computational Innovation (CCNI) at RPI.

REFERENCES

- (1) Melander, W. R.; El Rassi, Z.; Horváth, C. Interplay of Hydrophobic and Electrostatic Interactions in Biopolymer Chromatography: Effect of Salts on the Retention of Proteins. *J. Chromatogr.* A 1989, 469, 3–27.
- (2) Cramer, S. M.; Holstein, M. A. Downstream Bioprocessing: Recent Advances and Future Promise. *Curr. Opin. Chem. Eng.* **2011**, *1*, 27–37.
- (3) Ghose, S.; Hubbard, B.; Cramer, S. M. Protein Interactions in Hydrophobic Charge Induction Chromatography (HCIC). *Biotechnol. Prog.* **2005**, *21*, 498–508.
- (4) Johansson, B.-L.; Belew, M.; Eriksson, S.; Glad, G.; Lind, O.; Maloisel, J.-L.; Norrman, N. Preparation and Characterization of Prototypes for Multi-Modal Separation Media Aimed for Capture of Negatively Charged Biomolecules at High Salt Conditions. *J. Chromatogr. A* 2003, 1016, 21–33.
- (5) Burton, S. C.; Haggarty, N. W.; Harding, D. R. K. One Step Purification of Chymosin by Mixed Mode Chromatography. *Biotechnol. Bioeng.* 1997, 56, 45–55.
- (6) Burton, S. C.; Harding, D. R. K. High-Density Ligand Attachment to Brominated Allyl Matrices and Application to Mixed Mode Chromatography of Chymosin. *J. Chromatogr. A* **1997**, 775, 39–50.
- (7) Holstein, M. A.; Parimal, S.; McCallum, S. A.; Cramer, S. M. Mobile Phase Modifier Effects in Multimodal Cation Exchange Chromatography. *Biotechnol. Bioeng.* **2012**, *109*, 176–186.
- (8) Woo, J. A.; Chen, H.; Snyder, M. A.; Chai, Y.; Frost, R. G.; Cramer, S. M. Defining the Property Space for Chromatographic

- Ligands from a Homologous Series of Mixed-Mode Ligands. *J. Chromatogr. A* **2015**, *1407*, 58–68.
- (9) Woo, J.; Parimal, S.; Brown, M. R.; Heden, R.; Cramer, S. M. The Effect of Geometrical Presentation of Multimodal Cation-Exchange Ligands on Selective Recognition of Hydrophobic Regions on Protein Surfaces. *J. Chromatogr. A* **2015**, *1412*, 33–42.
- (10) Robinson, J.; Snyder, M. A.; Belisle, C.; Liao, J.; Chen, H.; He, X.; Xu, Y.; Cramer, S. M. Investigating the Impact of Aromatic Ring Substitutions on Selectivity for a Multimodal Anion Exchange Prototype Library. *J. Chromatogr. A* **2018**, *1569*, 101–109.
- (11) Kaleas, K. A.; Schmelzer, C. H.; Pizarro, S. A. Industrial Case Study: Evaluation of a Mixed-Mode Resin for Selective Capture of a Human Growth Factor Recombinantly Expressed in E. Coli. *J. Chromatogr. A* **2010**, *1217*, 235–242.
- (12) Kaleas, K. A.; Tripodi, M.; Revelli, S.; Sharma, V.; Pizarro, S. A. Evaluation of a Multimodal Resin for Selective Capture of CHO-Derived Monoclonal Antibodies Directly from Harvested Cell Culture Fluid. *J. Chromatogr. B* **2014**, *969*, 256–263.
- (13) Clarkson, J.; Campbell, I. D. Studies of Protein-Ligand Interactions by NMR. *Biochem. Soc. Trans.* **2003**, *31*, 1006–1009.
- (14) Lu, R. C.; Guo, X. R.; Jin, C.; Xiao, J. X. NMR Studies on Binding Sites and Aggregation-Disassociation of Fluorinated Surfactant Sodium Perfluorooctanoate on Protein Ubiquitin. *Biochim. Biophys. Acta, Gen. Subj.* **2009**, *1790*, 134–140.
- (15) Hong, Y.-H.; Ahn, H.-C.; Lim, J.; Kim, H.-M.; Ji, H.-Y.; Lee, S.; Kim, J.-H.; Park, E. Y.; Song, H. K.; Lee, B.-J. Identification of a Novel Ubiquitin Binding Site of STAM1 VHS Domain by NMR Spectroscopy. *FEBS Lett.* **2009**, *583*, 287–292.
- (16) Williamson, M. P. Progress in Nuclear Magnetic Resonance Spectroscopy Using Chemical Shift Perturbation to Characterise Ligand Binding. *Prog. Nucl. Magn. Reson. Spectrosc.* **2013**, 73, 1–16.
- (17) Holstein, M. A.; Chung, W. K.; Parimal, S.; Freed, A. S.; Barquera, B.; McCallum, S. A.; Cramer, S. M. Probing Multimodal Ligand Binding Regions on Ubiquitin Using Nuclear Magnetic Resonance, Chromatography, and Molecular Dynamics Simulations. *J. Chromatogr. A* 2012, 1229, 113–120.
- (18) Chung, W. K.; Freed, A. S.; Holstein, M. A.; McCallum, S. A.; Cramer, S. M. Evaluation of Protein Adsorption and Preferred Binding Regions in Multimodal Chromatography Using NMR. *Proc. Natl. Acad. Sci. U.S.A.* **2010**, *107*, 16811–16816.
- (19) Holstein, M. A.; Parimal, S.; McCallum, S. A.; Cramer, S. M. Effects of Urea on Selectivity and Protein–Ligand Interactions in Multimodal Cation Exchange Chromatography. *Langmuir* **2013**, 29, 158–167.
- (20) Engel, M. F. M.; Visser, A. J. W. G.; van Mierlo, C. P. M. Conformation and Orientation of a Protein Folding Intermediate Trapped by Adsorption. *Proc. Natl. Acad. Sci. U.S.A* **2004**, *101*, 11316–11321.
- (21) Gagner, J. E.; Lopez, M. D.; Dordick, J. S.; Siegel, R. W. Effect of Gold Nanoparticle Morphology on Adsorbed Protein Structure and Function. *Biomaterials* **2011**, *32*, 7241–7252.
- (22) Shrivastava, S.; Mccallum, S. A.; Nuffer, J. H.; Qian, X.; Siegel, R. W.; Dordick, J. S. Identifying Specific Protein Residues That Guide Surface Interactions and Orientation on Silica Nanoparticles. *Langmuir* 2013, 29, 10841–10849.
- (23) Tollefson, E. J.; Allen, C. R.; Chong, G.; Zhang, X.; Rozanov, N. D.; Bautista, A.; Cerda, J. J.; Pedersen, J. A.; Murphy, C. J.; Carlson, E. E.; et al. Preferential Binding of Cytochrome c to Anionic Ligand-Coated Gold Nanoparticles: A Complementary Computational and Experimental Approach. ACS Nano 2019, 13, 6856–6866.
- (24) You, C.-C.; De, M.; Han, G.; Rotello, V. M. Tunable Inhibition and Denaturation of R-Chymotrypsin with Amino Acid-Functionalized Gold Nanoparticles. *J. Am. Chem. Soc.* **2005**, *127*, 12873–12881.
- (25) De, M.; You, C.-C.; Srivastava, S.; Rotello, V. M. Biomimetic Interactions of Proteins with Functionalized Nanoparticles: A Thermodynamic Study. *J. Am. Chem. Soc.* **2007**, *129*, 10747–10753. (26) Srinivasan, K.; Parimal, S.; Lopez, M. M.; McCallum, S. A.;
- (26) Srinivasan, K.; Parimal, S.; Lopez, M. M.; McCallum, S. A.; Cramer, S. M. Investigation into the Molecular and Thermodynamic

- Basis of Protein Interactions in Multimodal Chromatography Using Functionalized Nanoparticles. *Langmuir* **2014**, *30*, 13205–13216.
- (27) Yao, Y.; Lenhoff, A. M. Electrostatic Contributions to Protein Retention in Ion-Exchange Chromatography. 1. Cytochrome c Variants. *Anal. Chem.* **2004**, *59*, No. 6743.
- (28) Dismer, F.; Hubbuch, J. A Novel Approach to Characterize the Binding Orientation of Lysozyme on Ion-Exchange Resins. *J. Chromatogr. A* **2007**, *1149*, 312–320.
- (29) Dismer, F.; Petzold, M.; Hubbuch, J. Effects of Ionic Strength and Mobile Phase PH on the Binding Orientation of Lysozyme on Different Ion-Exchange Adsorbents. *J. Chromatogr. A* **2008**, *1194*, 11–21.
- (30) Chung, W. K.; Holstein, M. A.; Freed, A. S.; Evans, S. T.; Baer, Z. C.; Cramer, S. M. Ion Exchange Chromatographic Behavior of a Homologous Cytochrome C Variant Library Obtained by Controlled Succinylation. *Sep. Sci. Technol.* **2010**, *45*, 2144–2152.
- (31) Chung, W. K.; Evans, S. T.; Freed, A. S.; Keba, J. J.; Baer, Z. C.; Rege, K.; Cramer, S. M. Utilization of Lysozyme Charge Ladders to Examine the Effects of Protein Surface Charge Distribution on Binding Affinity in Ion Exchange Systems. *Langmuir* **2010**, *26*, 759–768.
- (32) Zhang, L.; Zhao, G.; Sun, Y. Molecular Insight into Protein Conformational Transition in Hydrophobic Charge Induction Chromatography: A Molecular Dynamics Simulation. *J. Phys. Chem. B* **2009**, *113*, 6873–6880.
- (33) Yu, G.; Liu, J.; Zhou, J. Mesoscopic Coarse-Grained Simulations of Hydrophobic Charge Induction Chromatography (HCIC) for Protein Purification. *AIChE J.* **2015**, *61*, 2035–2047.
- (34) Parimal, S.; Garde, S.; Cramer, S. M. Effect of Guanidine and Arginine on Protein–Ligand Interactions in Multimodal Cation-Exchange Chromatography. *Biotechnol. Prog.* **2017**, *33*, 435–447.
- (35) Parimal, S.; Garde, S.; Cramer, S. M. Interactions of Multimodal Ligands with Proteins: Insights into Selectivity Using Molecular Dynamics Simulations. *Langmuir* **2015**, *31*, 7512–7523.
- (36) Freed, A. S.; Garde, S.; Cramer, S. M. Molecular Simulations of Multimodal Ligand-Protein Binding: Elucidation of Binding Sites and Correlation with Experiments. *J. Phys. Chem. B* **2011**, *115*, 13320–13327
- (37) Srinivasan, K.; Banerjee, S.; Parimal, S.; Sejergaard, L.; Berkovich, R.; Barquera, B.; Garde, S.; Cramer, S. M. Single Molecule Force Spectroscopy and Molecular Dynamics Simulations as a Combined Platform for Probing Protein Face-Specific Binding. *Langmuir* 2017, 33, 10851–10860.
- (38) Robinson, J.; Roush, D.; Cramer, S. Domain Contributions to Antibody Retention in Multimodal Chromatography Systems. *J. Chromatogr. A* **2018**, *1563*, 89–98.
- (39) Robinson, J.; Roush, D.; Cramer, S. M. The Effect of PH on Antibody Retention in Multimodal Cation Exchange Chromatographic Systems. *J. Chromatogr. A* **2020**, *1617*, No. 460838.
- (40) Gagnon, P.; Cheung, C.-W.; Yazaki, P. J. Cooperative Multimodal Retention of IgG, Fragments, and Aggregates on Hydroxyapatite. *J. Sep. Sci.* **2009**, *32*, 3857–3865.
- (41) Lin, D.-Q.; Tong, H.-F.; Wang, H.-Y.; Yao, S.-J. Molecular Insight into the Ligand–IgG Interactions for 4-Mercaptoethyl-Pyridine Based Hydrophobic Charge-Induction Chromatography. *J. Phys. Chem. B* **2012**, *116*, 1393–1400.
- (42) Tong, H.-F.; Cavallotti, C.; Yao, S.-J.; Lin, D.-Q. Molecular Insight into Protein Binding Orientations and Interaction Modes on Hydrophobic Charge-Induction Resin. *J. Chromatogr. A* **2017**, *1512*, 34–42
- (43) Gudhka, R. B.; Bilodeau, C. L.; McCallum, S. A.; McCoy, M. A.; Roush, D. J.; Snyder, M. A.; Cramer, S. M. Identification of Preferred Multimodal Ligand-binding Regions on IgG1 F C Using Nuclear Magnetic Resonance and Molecular Dynamics Simulations. *Biotechnol. Bioeng.* **2021**, *118*, 809–822.
- (44) Bilodeau, C. L.; Lau, E. Y.; Roush, D.; Garde, S.; Cramer, S. M. Formation of Ligand Clusters on Multimodal Chromatographic Surfaces. *Langmuir* **2019**, *35*, 16770–16779.

- (45) Jana, N. R.; Gearheart, L.; Murphy, C. J. Seeding Growth for Size Control of 5–40 Nm Diameter Gold Nanoparticles. *Langmuir* **2001**, *17*, 6782–6786.
- (46) Rule, G. S.; Hitchens, T. K. Fundamentals of Protein NMR Spectroscopy; Springer: Dordrecht, Netherlands, 2005.
- (47) DeLano, W. L. The PyMOL Molecular Graphics System, version 2.3; Schrödinger LLC, 2020.
- (48) Baker, N. A.; Sept, D.; Joseph, S.; Holst, M. J.; McCammon, J. A. Electrostatics of Nanosystems: Application to Microtubules and the Ribosome. *Proc. Natl. Acad. Sci. U.S.A.* **2001**, 98, 10037–10041.
- (49) Chennamsetty, N.; Voynov, V.; Kayser, V.; Helk, B.; Trout, B. L. Prediction of Aggregation Prone Regions of Therapeutic Proteins. *J. Phys. Chem. B* **2010**, *114*, 6614–6624.
- (50) Wang, J.; Cieplak, P.; Kollman, P. A. How Well Does a Restrained Electrostatic Potential (RESP) Model Perform in Calculating Conformational Energies of Organic and Biological Molecules? J. Comput. Chem. 2000, 21, 1049–1074.
- (51) Ponder, J. W.; Case, D. A. Force Fields for Protein Simulations. In *Protein Simulations*; Elsevier, 2003; Vol. 66, pp 27–85.
- (52) Shenogina, N.; Godawat, R.; Keblinski, P.; Garde, S. How Wetting and Adhesion Affect Thermal Conductance of a Range of Hydrophobic to Hydrophilic Aqueous Interfaces. *Phys. Rev. Lett.* **2009**, *102*, No. 156101.
- (53) Banerjee, S.; Parimal, S.; Cramer, S. M. A Molecular Modeling Based Method to Predict Elution Behavior and Binding Patches of Proteins in Multimodal Chromatography. *J. Chromatogr. A* **2017**, *1511*, 45–58.
- (54) Godawat, R.; Jamadagni, S. N.; Garde, S. Characterizing Hydrophobicity of Interfaces by Using Cavity Formation, Solute Binding, and Water Correlations. *Proc. Natl. Acad. Sci. U.S.A.* **2009**, *106*, 15119–15124.
- (55) Jamadagni, S. N.; Godawat, R.; Dordick, J. S.; Garde, S. How Interfaces Affect Hydrophobically Driven Polymer Folding. *J. Phys. Chem. B* **2009**, *113*, 4093–4101.
- (56) Wang, J.; Wolf, R. M.; Caldwell, J. W.; Kollman, P. A.; Case, D. A. Development and Testing of a General Amber Force Field. *J. Comput. Chem.* **2004**, *25*, 1157–1174.
- (57) Jakalian, A.; Bush, B. L.; Jack, D. B.; Bayly, C. I. Fast, Efficient Generation of High-Quality Atomic Charges. AM1-BCC Model: I. Method. *J. Comput. Chem.* **2000**, *21*, 132–146.
- (58) Love, J. C.; Estroff, L. A.; Kriebel, J. K.; Nuzzo, R. G.; Whitesides, G. M. Self-Assembled Monolayers of Thiolates on Metals as a Form of Nanotechnology. *Chem. Rev.* **2005**, *105*, 1103–1170.
- (59) Huggins, D. J. Correlations in Liquid Water for the TIP3P-Ewald, TIP4P-2005, TIP5P-Ewald, and SWM4-NDP Models. *J. Chem. Phys.* **2012**, *136*, No. 064518.
- (60) Abraham, M. J.; Murtola, T.; Schulz, R.; Páll, S.; Smith, J. C.; Hess, B.; Lindahl, E. GROMACS: High Performance Molecular Simulations through Multi-Level Parallelism from Laptops to Supercomputers. *SoftwareX* **2015**, *1*–2, 19–25.
- (61) Evans, D. J.; Holian, B. L. The Nose-Hoover Thermostat. J. Chem. Phys. 1985, 83, 4069-4074.
- (62) Parrinello, M.; Rahman, A. Crystal Structure and Pair Potentials: A Molecular-Dynamics Study. *Phys. Rev. Lett.* **1980**, *45*, 1196–1199.
- (63) Darden, T.; York, D.; Pedersen, L. Particle Mesh Ewald: An N-log(N) Method for Ewald Sums in Large Systems. *J. Chem. Phys.* 1993, 98, 10089–10092.
- (64) Srinivasan, K.; Banerjee, S.; Parimal, S.; Sejergaard, L.; Berkovich, R.; Barquera, B.; Garde, S.; Cramer, S. M. Single Molecule Force Spectroscopy and Molecular Dynamics Simulations as a Combined Platform for Probing Protein Face-Specific Binding. *Langmuir* **2017**, 33, 10851–10860.
- (65) Kumar, S.; Rosenberg, J. M.; Bouzida, D.; Swendsen, R. H.; Kollman, P. A. THE Weighted Histogram Analysis Method for Free-Energy Calculations on Biomolecules. I. The Method. *J. Comput. Chem.* **1992**, *13*, 1011–1021.

- (66) Souaille, M.; Roux, B. Extension to the Weighted Histogram Analysis Method: Combining Umbrella Sampling with Free Energy Calculations. *Comput. Phys. Commun.* **2001**, *135*, 40–57.
- (67) Hub, J. S.; de Groot, B. L.; van der Spoel, D. G_wham—A Free Weighted Histogram Analysis Implementation Including Robust Error and Autocorrelation Estimates. *J. Chem. Theory Comput.* **2010**, *6*, 3713–3720.
- (68) Humphrey, W.; Dalke, A.; Schulten, K. VMD: Visual Molecular Dynamics. J. Mol. Graph. 1996, 14, 33–38.
- (69) Gudhka, R. B.; Roush, D. J.; Cramer, S. M. A Thermodynamic Evaluation of Antibody-Surface Interactions in Multimodal Cation Exchange Chromatography. *J. Chromatogr. A* **2020**, *1628*, No. 461479.
- (70) Rajamani, S.; Truskett, T. M.; Garde, S. Hydrophobic Hydration from Small to Large Lengthscales: Understanding and Manipulating the Crossover. *Proc. Natl. Acad. Sci. U.S.A.* **2005**, *102*, 9475–9480.
- (71) Lum, K.; Chandler, D.; Weeks, J. D. Hydrophobicity at Small and Large Length Scales. *J. Phys. Chem. B* **1999**, *103*, 4570–4577.
- (72) Chandler, D. Interfaces and the Driving Force of Hydrophobic Assembly. *Nature* **2005**, 437, 640–647.